POLITECNICO DI TORINO

Master of Science in Mechanical Engineering

MASTER'S DEGREE THESIS

Additive Manufacturing of Ceramic Materials for Microelectronics Applications

Supervisors:

Prof. Luciano Scaltrito
Prof. Valentina Bertana

Candidate:

Ali Reza Azizi

July 2025

Abstract

This thesis investigates the additive manufacturing of alumina ceramic components using Digital Light Processing (DLP), with a focus on applications in microelectronics and thermal management systems. As demand increases for miniaturized, high-performance ceramic parts, vat photopolymerization (VPP) has emerged as a promising technology for producing complex geometries with high dimensional fidelity. However, challenges persist in controlling exposure parameters, minimizing interlayer defects, and ensuring robust mechanical and thermal properties in the sintered components.

To address these issues, a material shaping workflow was implemented using AdmaPrint A130 slurry and a DLP system. Post-processing involved ultrasonic TPM solvent cleaning, debinding, and sintering. The produced samples were characterized through dimensional shrinkage analysis, porosity evaluation via Archimedes' method, mechanical testing through three-point bending, and thermal conductivity measurements.

The results demonstrated consistent volumetric shrinkage (~55.9%), low open porosity (~1.25%), and reliable mechanical performance, with an average flexural strength of 228.1 MPa and Young's modulus of 221.6 GPa. Thermal conductivity ranged from 1.98 to 2.44 W/m·K over the 100–250 °C range, with steady-state heat flux confirmed during testing.

In the final phase, a numerically simulated case study was performed to assess the performance of a custom-designed alumina thermal dissipator. The model incorporated realistic boundary conditions and fluid–solid thermal interaction, showing significant thermal resistance across the ceramic and highlighting areas for design optimization, such as thickness reduction and improved channel geometry.

This work validates the potential of DLP-fabricated alumina ceramics for both structural and thermal functions, and establishes a reproducible, digitally integrated workflow that bridges laboratory experimentation with industrial application.

Table of Contents

List of Figures

List of Tables

1 Introduction

1.1 Additive Manufacturing

Additive Manufacturing (AM), commonly referred to as 3D printing, originated in the 1980s to support rapid prototyping and has since developed into a key technology within modern manufacturing (1)**.** AM builds objects layer by layer from CAD models, enabling the creation of geometrically complex and highly customizable parts. In contrast, Subtractive Manufacturing (SM) removes material from a solid block, often resulting in greater material waste and geometric constraints (2,3) .

To illustrate the comparative advantages of AM over SM, Table 1 presents a summary of key differences.

Table 1. Comparison between Additive and Subtractive Manufacturing (2,3)

Feature	Additive Manufacturing (AM)	Subtractive Manufacturing (SM)
Material usage	Minimal waste, efficient use	High material loss
Design complexity	Excellent for complex/internal geometries	Limited by tool access and path
Setup cost for *a* small series	Low	High
Surface finish (as printed)	Moderate needs post-processing	Excellent, directly from machining
Suitability for ceramics	High, especially DLP with alumina	Poor ceramics are brittle and hard to machine
Customization & flexibility	High, easy CAD-to-part transition	Low, retooling required for new designs

Given the rising demand for miniaturized, lightweight, and high-performance components in sectors such as microelectronics, biomedicine, aerospace, and can further be used in the jewelry and construction industries. AM, particularly through Digital Light Processing, has emerged as an effective technique. It enables the fabrication of complex parts with improved material efficiency, shorter production cycles, and reduced tooling constraints. (4–8)

According to the ISO/ASTM 52900:2021 standard, Additive Manufacturing (AM) is categorized into seven primary process types: vat photopolymerization, material extrusion, material jetting, binder jetting, powder bed fusion, directed energy deposition, and sheet lamination (9–11) (Fig.1).

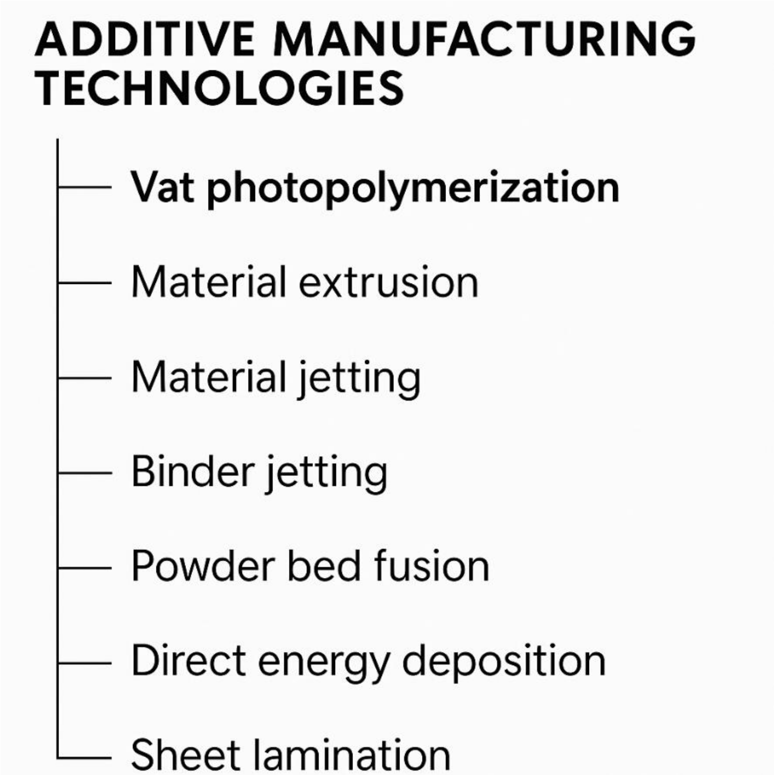

Figure 1. Division of the additive manufacturing technologies according to ISO/ASTM 52900:2021 (9)

Among these, Vat Photopolymerization (VPP) stands out as a leading method for high-resolution printing, especially for ceramic components, due to its exceptional layer precision and capability to form complex geometries (12,13).

In VPP, a light source selectively cures a liquid photopolymer resin layer in a layer-by-layer process. The specific method of light delivery determines the VPP subtype:

- Stereolithography (SLA): a focused UV laser scans and cures point-by-point (14) .
- Digital Light Processing (DLP): A projector cures an entire layer at once using a DMD (digital micromirror device) (15,16) .
- Continuous Digital Light Processing (CDLP/CLIP): a continuous curing method that uses LED light combined with oxygen control to allow uninterrupted part growth (17–22) **.**

These technologies are schematically compared below:

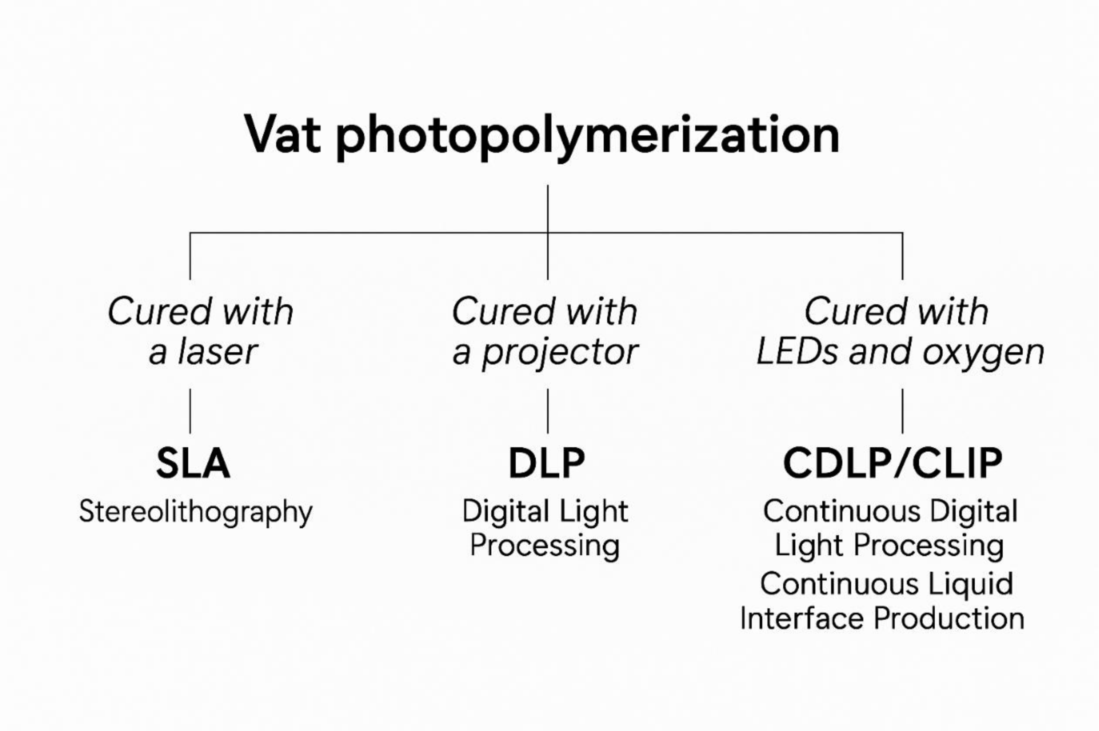

Figure 2. Classification of VP based on curing method. (17)

1.1.1 Digital Light Processing – DLP

Among the VPP techniques, DLP has become one of the most suitable methods for additive manufacturing because it can be used to fabricate a single layer of a 3D object through selective solidification using a projector light (either UV or white light). In this way, a layer can be formed rapidly(23,24). Its main advantages include high resolution, fast printing speed, and good compatibility with ceramic slurries. Unlike SLA, which uses a laser to cure each point one by one, DLP projects an entire layer of UV light all at once using a DMD. This makes the process faster and more precise (25–27) A standard DLP setup includes:

- A transparent vat filled with a ceramic-resin slurry
- A UV projector that displays the pattern of each layer
- A build plate that moves vertically to create the part layer by layer

A typical DLP setup is shown in Figure 3.

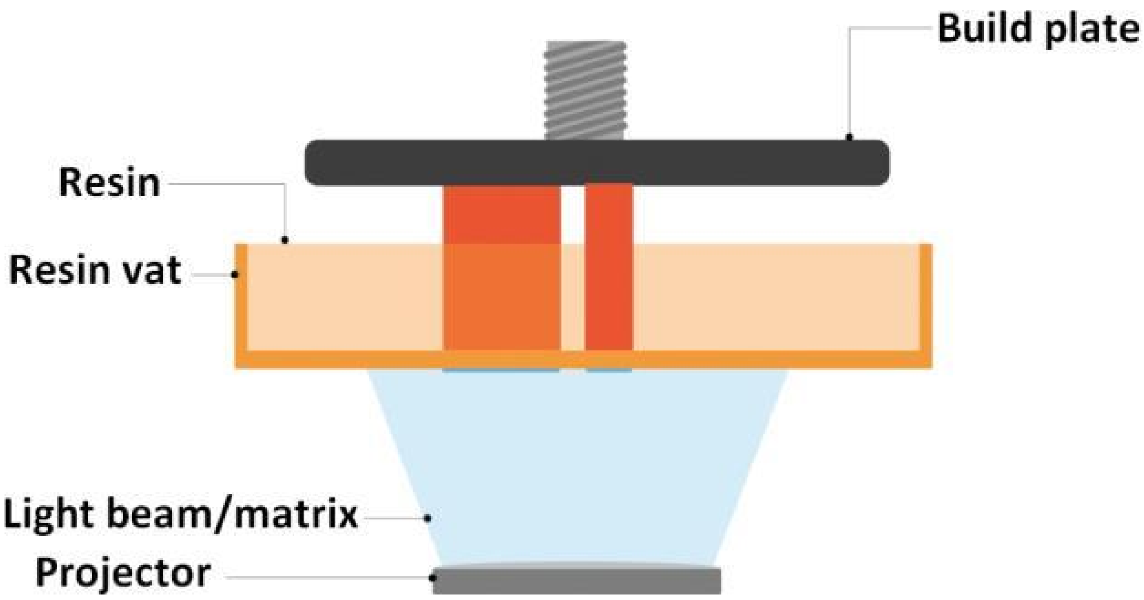

Figure 3. Schematic diagram of DLP technology (25)

1.2 Materials for Vat Photopolymerization Process: DLP Resins

VPP processes for additive manufacturing rely on the light irradiation for cutting the photo-polymeric resin. The choice of materials significantly impacts not only the printability and resolution of the final component but also its final physical characteristics. In DLP, which is classified under VPP, ceramic powders, such as alumina, are dispersed into a liquid photosensitive resin to form a homogeneous slurry. This slurry must maintain stable flow behavior and allow for efficient light penetration and curing (28–31).

The resin formulation is critical to the success of DLP printing. A typical resin bath consists of:

- Monomers and oligomers (e.g., acrylates or methacrylates)
- Photoinitiators (to trigger polymerization upon UV exposure)
- Dispersants (to prevent agglomeration of ceramic particles)
- Rheology modifiers (to control viscosity and flow behavior) (32–35).

Upon UV light exposure—typically in the 365–405 nm range—photoinitiators absorb energy and decompose to produce reactive free radicals. These radicals initiate the cross-linking of monomers and oligomers, forming a stable polymer network. This photopolymerization process is irreversible: once cured, the material cannot revert to its liquid state (36–39).

The core polymerization mechanism and general DLP slurry composition are illustrated in the following figures:

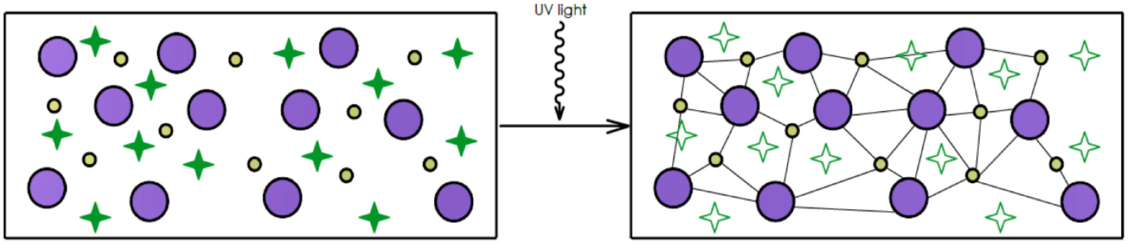

Figure 4. Liquid photopolymer (on the left), induced polymerization by light (small circle—monomer, large circle—oligomer, star—photo initiator)(28)

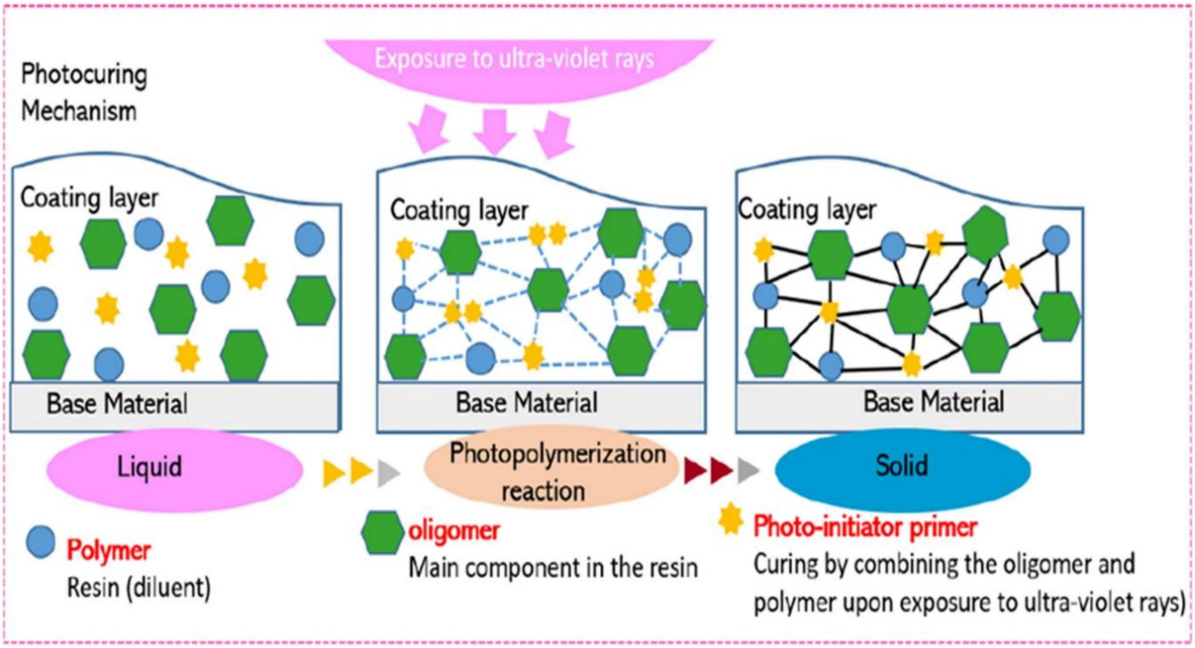

Figure 5. A schematic representation of the fundamental polymer structure, showcasing cross-linked oligomers that are cured through ultraviolet light activation and a photoinitiator primer (38)

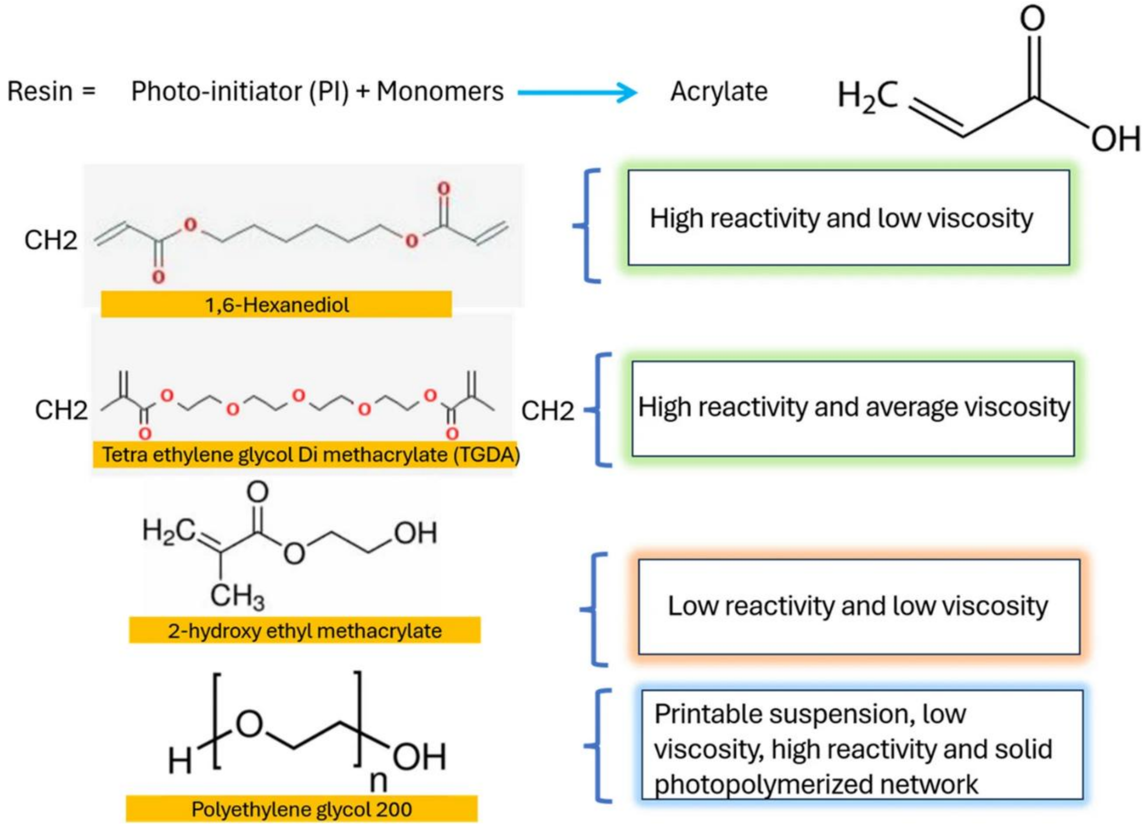

Figure 6. A schematic illustrating the selection of monomers and photo initiators based on the free radicals generated during slurry suspension preparation. (38)

These resin systems must be carefully tuned to maintain low viscosity, enable high solid loading, and ensure light transparency. Poor formulation can lead to weak layer adhesion, low resolution, and defects (40).

1.3 Ceramic Materials

Ceramics, derived from the Greek word Keramicos, meaning "burnt material," are inorganic, non-metallic materials typically formed through ionic or covalent bonds between metallic and non-metallic elements (41) , (42) They are renowned for their:

- High hardness
- Thermal resistance
- Low density
- Chemical inertness
- Mechanical strength

Ceramics are broadly divided into:

- Traditional ceramics, such as porcelain, brick, and tile

- Advanced ceramics, including oxides, carbides, and nitrides tailored for engineering applications

In the context of additive manufacturing, ceramics are typically grouped into three categories: oxides, non-oxides, and composite ceramics. This classification is illustrated in the following Figure 7: (43,44)

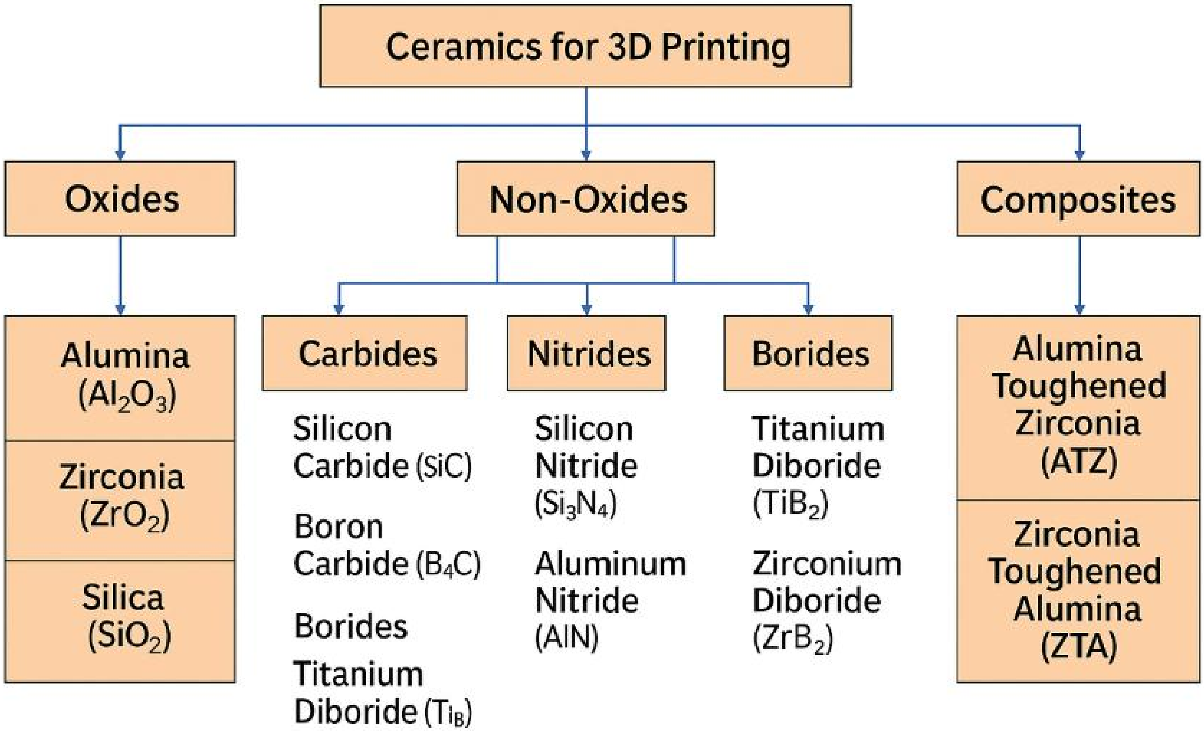

Figure 7. Classification of ceramic materials used in additive manufacturing (43)(44)

In photopolymer-based AM processes like DLP and SLA, finely dispersed ceramic powders are suspended in UV-curable polymers (45) . The selection of powder affects the printability, cure depth, and sintering behavior. Table 2 summarizes the most used ceramic materials in this context (46) .

Table 2: Common Ceramic Materials and Their Chemical Formulas (46)

Material	**Chemical Formula**
Aluminum Oxide	Al_2O_3
Zirconium Dioxide	ZrO_2
Silica	SiO_2
Tungsten Carbide	WC
Boron Nitride	BN
Aluminum Nitride	AlN
Silicon Carbide	SiC
Boron Carbide	B_4C
Titanium Diboride	TiB_2

1.3.1 Ceramic materials: Alumina

Alumina (Al_2O_3) is one of the most widely studied ceramics in additive manufacturing, thanks to its excellent mechanical strength, thermal stability, chemical resistance, and electrical insulation. It is extensively used in microelectronics, biomedical implants, and aerospace components. The advancement of DLP-based printing has enabled the fabrication of complex alumina parts with superior dimensional precision and minimal material waste (47–51)**.**

Figure 8. Alumina ceramic substrates used in microelectronic applications due to their high thermal conductivity, electrical insulation, and mechanical reliability (47)

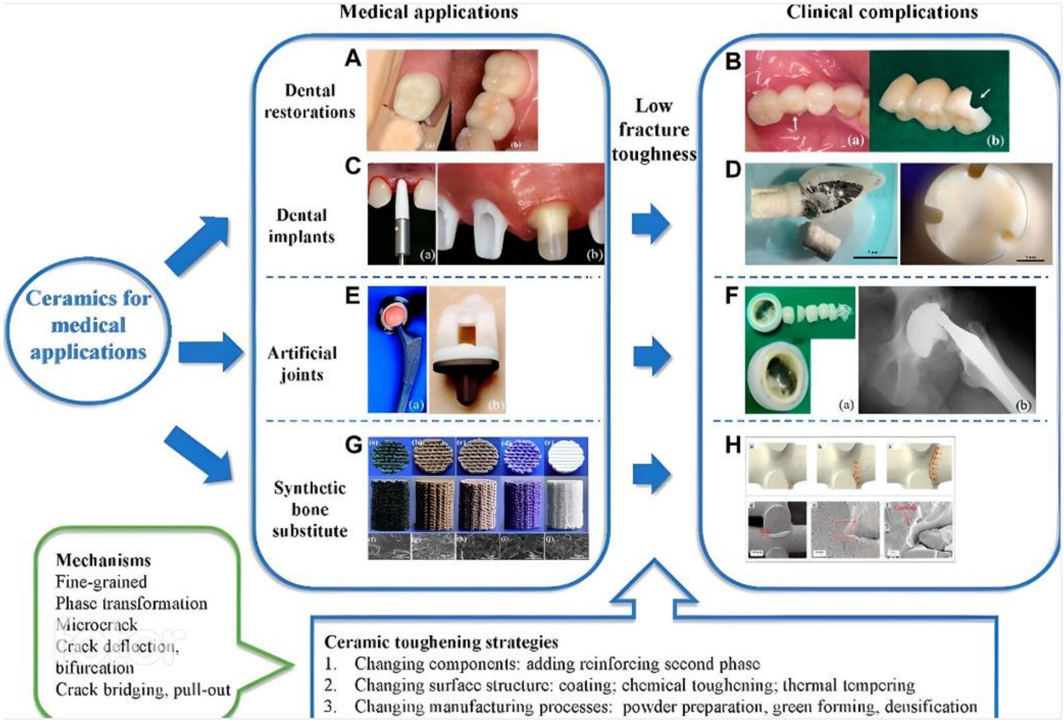

Figure 9. Various biomedical applications of alumina ceramics, including dental restorations, artificial joints, and bone substitutes, highlight the material's biocompatibility and mechanical strength. (48)

1.4 CerAM technologies: VPP

In ceramic AM, the manufacturing stages for obtaining the final product are:

- Raw material calcination and milling, to obtain a final powder with the desired composition and grain dimensions.
- Feedstock/starting material preparation, which implies the taw powder mixing with the selected binder system, compatible with the chosen CerAM technology.
- Material shaping, to fabricate the green body with desired geometrical characteristics, using the more adequate CerAM technology.
- Solvent cleaning, to remove excess starting materials.
- Debinding, which can be thermal or solvent-based, aims to eliminate the organic binder matrix.
- Sintering (typically 1500–1650 °C for alumina) to densify the ceramic and develop its final properties(52).

The importance of each post-processing step cannot be overestimated. Solvent cleaning ensures the removal of residual organics that could cause defects during the sintering process. Improper debinding can result in cracking, delamination, or deformation due to rapid release of gas or uneven thermal gradients. (53,54)

Therefore, debinding schedules often employ slow heating ramps and hold times to promote uniform decomposition of the binder phase (55) **.**

Sintering is the final and most critical step. Alumina green bodies are typically sintered between 1550 and 1650 °C, which leads to densification, grain boundary formation, and microstructural evolution. Shrinkage during sintering—often in the range of 15–25%—must be accounted for in the CAD model. Final properties such as strength, density, and dielectric performance depend on sintering temperature, dwell time, and heating/cooling rates (56) .

To better understand and classify ceramic AM technologies, the VDI 3405 Part 8.1 (2021) standard introduces two main classification criteria: (57)

- The form of the material (slurry, powder, paste, filament).

- The type of binder (photopolymer, thermoplastic, reactive, or water-based).

An overview of the CerAM classification, based on these two criteria, is presented in the table below (Table 3), while typical feature sizes obtained from these technologies are shown in the table below (Table 4).

Table 3. Additive manufacturing processes for ceramics and their characteristics (57)

AM Process	Starting Material	Material Application	Consolidation Mechanism
Material extrusion	Cold plastic	Selectively, string-shaped	Structural viscosity, gelation, drying, etc.
	Thermoplastic	Selectively, string-shaped	Cooling
	3D screen printing (suspension)	Selectively, planar	Structural viscosity and subsequent curing
Binder jetting	Powder, granules, suspension	Planar	Selectively via binder insertion
Vat photopolymerization	Standing suspension	Planar	Selective via light exposure unit
	Hanging suspension	Planar	Selective via light exposure unit
Material jetting	Solvent-based suspension	Selective, drop-shaped	Structural viscosity and subsequent drying
	Thermoplastic mass	Selective, drop-shaped	Structural viscosity and cooling

Table 4. Typical features of printed ceramic parts after sintering (57)

Process	**Part Size (x–y)**	**Z (max)**	**Wall Thickness (mm)**	**Layer Thickness (µm)**
Material extrusion	10–1000 mm	1000 mm	0.5–10	100–5000
Binder jetting	2–1000 mm	500 mm	0.2–100	10–200
Vat photopolymerization	0.5–500 mm	250–300 mm	0.1–1.5	5–100
Material jetting	0.5–200 mm	30–150 mm	0.1–1.5	~10–200

DLP fits under the category of slurry-based photopolymer systems, making it a good choice for printing technical ceramics with high resolution and complex shapes.

1.4.1 CerAM DLP for Alumina: Process flow and Application

Digital Light Processing (DLP) in ceramic additive manufacturing involves a structured workflow that includes material preparation, digital modeling, layer-by-layer fabrication, and thermal post-processing. For ceramics such as alumina, the CerAM DLP process enables the fabrication of high-resolution components with excellent dimensional accuracy and material efficiency. This section outlines the complete process, from digital design to final sintered parts, while highlighting the specific procedures required for ceramic post-processing (58,59).

The process begins with the generation of a 3D digital model using CAD software. This model is exported in STL format and sliced into thin 2D layers that correspond to the object's cross-sections. The DLP system uses these slices to project UV light patterns onto the resin surface (60) .

A ceramic slurry consisting of dispersed alumina particles in a UV-curable resin is loaded into a transparent vat. Depending on the printer configuration, the platform operates either Bottom-up or Top-down as each layer is sequentially cured. Once printing is complete, the green parts—composed of ceramic particles embedded in a polymer matrix—are removed from the platform for post-processing. (61) **.**

The complete process workflow is shown in Figure 10.

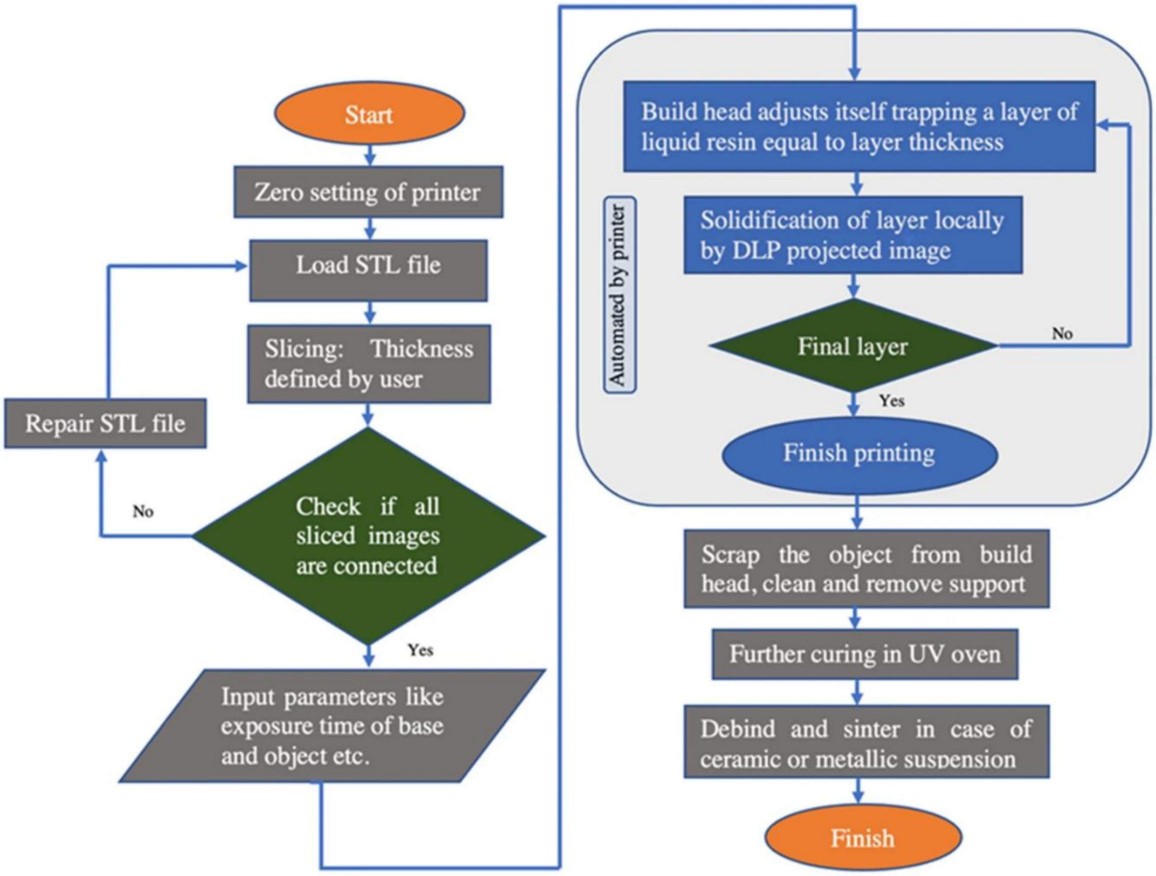

Figure 10. DLP process workflow from CAD model to sintered ceramic part (61)

1.4.2 Alumina-Based Resin

The key to successful DLP printing of ceramics lies in the careful formulation of photopolymerizable suspensions, which combine UV-curable organic monomers and oligomers with finely dispersed ceramic powders. These suspensions must be optimized to ensure smooth flow, efficient light curing, and minimal scattering. The ceramic slurry must strike a delicate balance between light absorption, viscosity, and homogeneity, as shown in Figure 11. (62–64) .

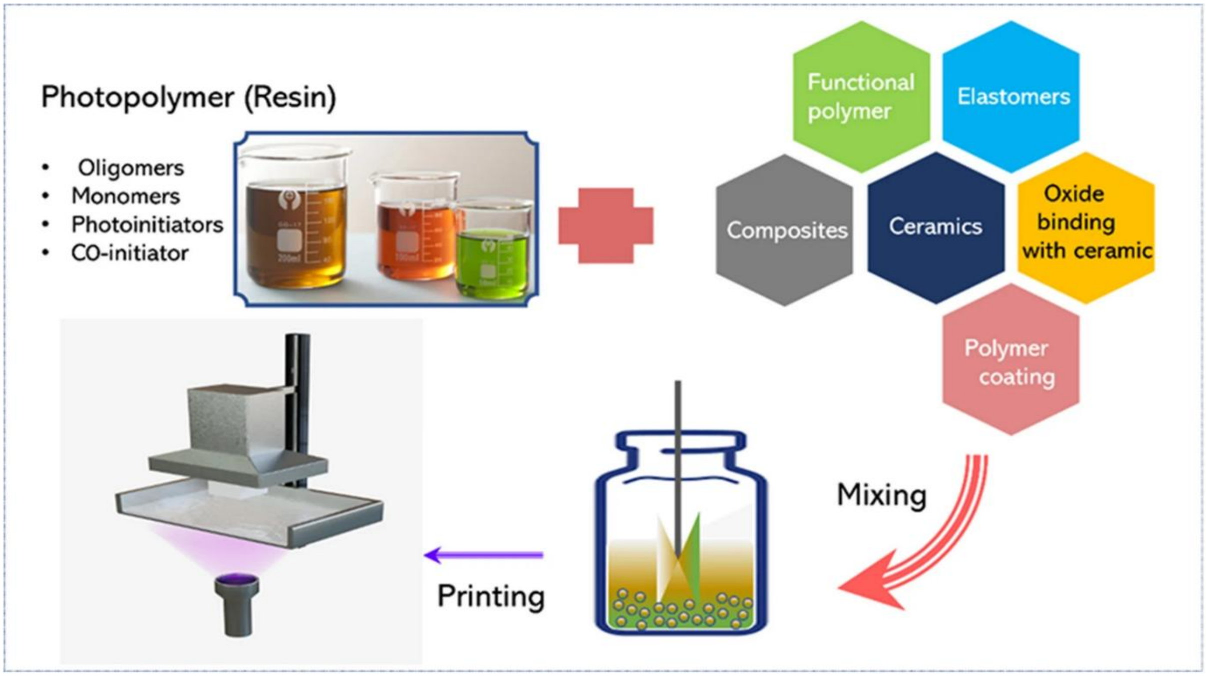

Figure 11. A schematic illustrating the photopolymerization process, including the typical composition of materials, slurry suspension preparation, and curing of the ceramic suspension during the DLP 3D printing process. (38)

An optimal ceramic suspension for DLP printing should possess low viscosity, shear-thinning behavior, and uniform particle dispersion to ensure smooth layer deposition and effective curing. High solid loadings—typically exceeding 40 vol%—are desirable for minimizing shrinkage and achieving better densification during sintering (65,66). However, excessive ceramic content may increase viscosity beyond printable limits and induce light scattering, which can negatively impact resolution and layer adhesion (67,68) .

Furthermore, the selection of monomers and photoinitiators must be optimized to ensure compatibility with ceramic powders, low viscosity, and complete polymerization without overcuring or unintended diffusion. The figures in Section 1.2 provide a detailed visual overview of the resin chemistry principles that also apply to alumina-based systems.

1.4.3 Application fields

Ceramic parts produced by DLP-based additive manufacturing are widely utilized in demanding applications where mechanical strength, chemical stability, dimensional precision, and electrical insulation are critical. Some key industrial fields include:

- Microelectronics: Alumina substrates are used in power module packaging, high-frequency circuit boards, and insulating layers due to their thermal conductivity and dielectric properties.
- Biomedical: Custom dental prosthetics, hip implants, and porous scaffolds benefit from the biocompatibility and structural integrity of sintered alumina.
- Aerospace and Energy: Ceramics serve as thermal barriers, structural reinforcements, and dielectric support in turbine components, sensors, and high-temperature insulators (69–71) .

The capability of DLP to fabricate complex geometries with high resolution enables component miniaturization, multifunctional integration, and lightweight optimization—essential for next-generation devices.

Recent advancements in DLP have enhanced ceramic AM in terms of microstructural control, porosity reduction, and mechanical performance. However, several challenges remain:

- Porosity control: Uneven light exposure can result in inconsistent curing, non-uniform porosity, and poor interlayer adhesion.
- Slurry formulation: Achieving high ceramic loading while ensuring stable dispersion remains complex.
- Exposure optimization: Few studies comprehensively link process parameters to resulting microstructure and part quality (61)

Low-rate vacuum debinding has been shown to reduce delamination and cracking during binder removal, while optimized sintering temperatures improve part density but may also result in excessive grain growth (72,73).

To address these open issues, this thesis investigates the impact of DLP exposure parameters on porosity, shrinkage, and structural performance in printed alumina components. The objective is to define exposure strategies that improve the mechanical integrity and reliability of functional parts (74) .

In support of this investigation, Figure 12 summarizes common defect types and pore classification schemes found in ceramic AM processes. While the figure is derived from extrusion-based AM, the types, such as sintered-related porosity, engineered voids, and trapped gases, also appear in light-based processes like DLP under improper curing or debinding conditions (75–77) .

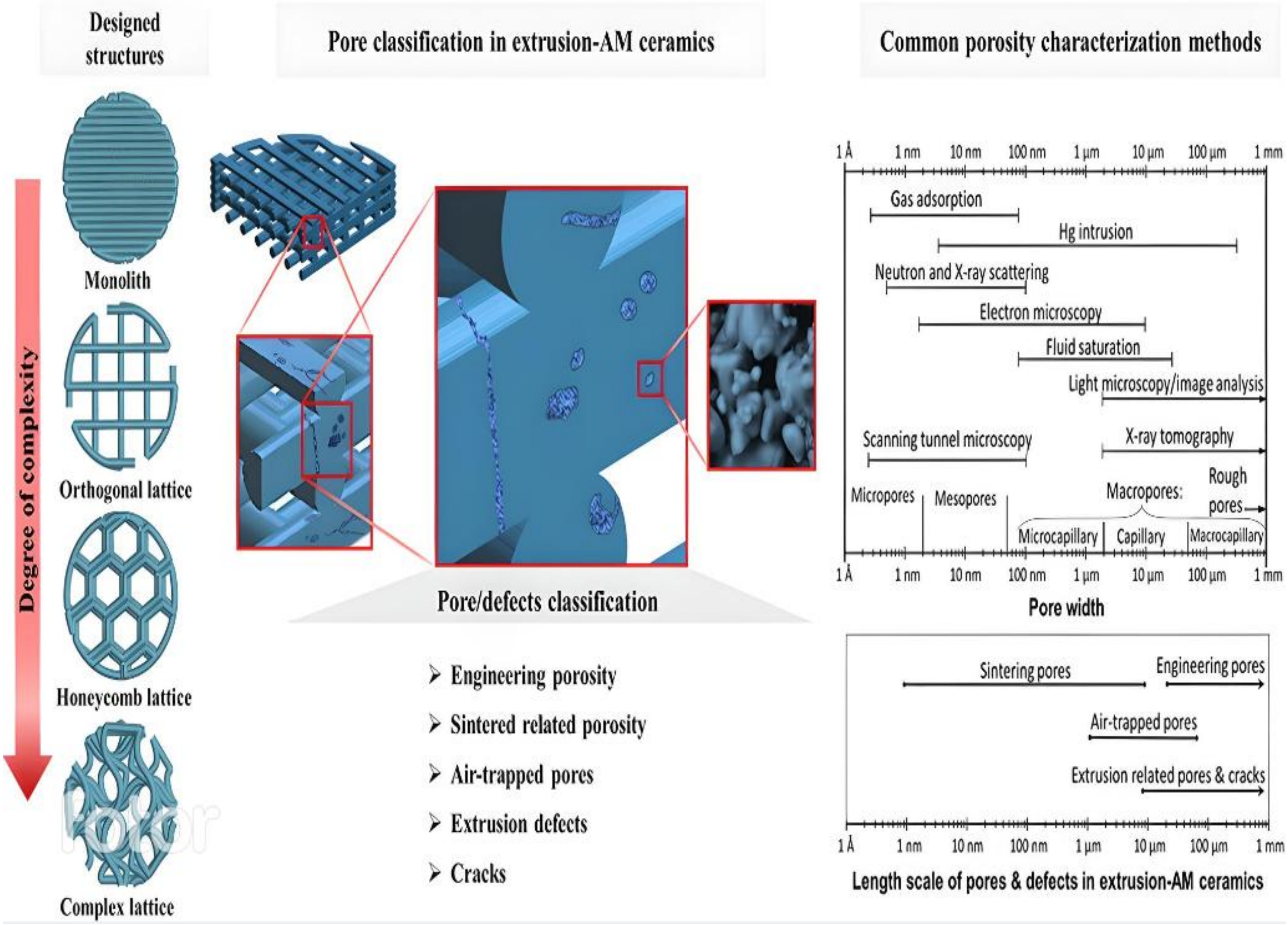

Figure 12. Schematic diagram illustrating various pore and defect types in extrusion-based ceramic additive manufacturing. Categories include engineered porosity, sintered-related porosity, air-trapped pores, extrusion defects, and cracks, observed in different lattice geometries.(72)

Comprehensive characterization was also performed on printed alumina samples to validate part quality. As shown in Figure 13, the green body appearance (a), sintered microstructure (b), and internal 3D geometry (c) were analyzed. Elemental composition was confirmed using Energy Dispersive X-ray Spectroscopy (EDS) (d), and XCT-based porosity mapping revealed a low pore volume fraction (e–f), indicating excellent densification. (78)

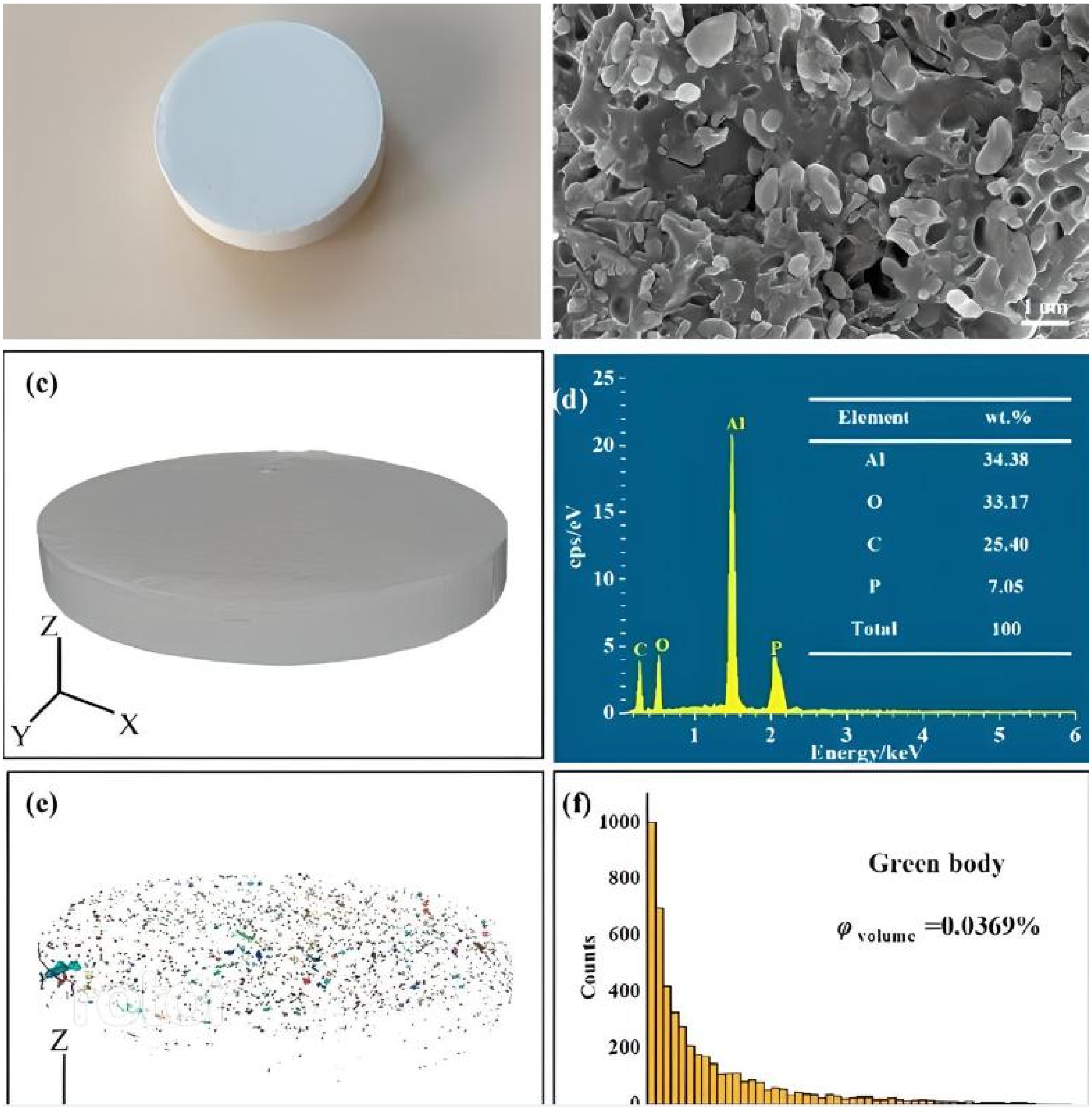

Element	wt.%
Al	34.38
O	33.17
C	25.40
P	7.05
Total	100

Figure 13. Morphological and compositional analysis of a DLP-printed alumina part. (a) Green body appearance; (b) SEM image showing sintered microstructure; (c) XCT 3D rendering; (d) EDS spectrum confirming alumina composition; (e) Porosity distribution visualization; (f) Histogram of pore volume fraction (φ = 0.0369%)(74)

These insights contribute to materials development efforts in microelectronics, biomedicine, and structural ceramics, where reliability, miniaturization, and advanced functionality are increasingly demanded.

1.5 Objectives and Scope

This research is focused on the characterization of a commercially available ceramic resin used in DLP-based additive manufacturing. The primary aim is to evaluate the resin's suitability for thermal management applications, specifically in power module systems where high thermal reliability is required. The study examines how variations in DLP light exposure parameters affect the porosity, dimensional fidelity, and mechanical performance of printed alumina components. By optimizing exposure strategies, the work seeks to enhance the functionality and structural reliability of ceramic parts produced via DLP.

Alumina was selected due to its widespread industrial relevance, particularly in applications requiring wear resistance, thermal stability, and biocompatibility. These include:

- Microelectronics, where alumina serves as an insulating substrate with good thermal conductivity.
- Biomedical implants, including dental and orthopedic components.
- Aerospace systems, where lightweight and heat-resistant materials are essential.

The methodological workflow includes:

- Designing and printing test geometries, followed by controlled variation of exposure parameters using DLP technology.
- Post-processing operations, such as solvent cleaning, thermal debinding, and sintering.
- Dimensional characterization and porosity evaluation of printed parts.
- Mechanical testing, using three-point bending experiments to assess flexural strength and calculate Young's modulus.
- Thermal testing, to evaluate heat resistance and thermal conductivity of the sintered parts under controlled heating conditions.

In the final phase of this research, a ceramic-based thermal dissipator was designed and simulated as a case study to explore the potential of DLP-printed alumina in thermal management applications, including those relevant to microelectronics and power electronics.

Thesis Structure Overview

The thesis presents a first chapter that provides the contextual foundation for the study, outlining the relevance of ceramic additive manufacturing and the motivation for utilizing DLP technology. It outlines the current state of the art, defines research objectives, and delineates the scope and intended outcomes of the investigation.

The second chapter describes the materials, experimental setups, and procedures employed throughout the research.

The third chapter presents the results obtained from experimental investigations. This includes quantitative data on dimensional accuracy, porosity, density, and shrinkage, along with analysis of mechanical and thermal performance.

The final chapter summarizes the principal findings of the study, discusses their implications in the context of ceramic additive manufacturing, and outlines the limitations encountered. Suggestions for future research directions are also provided.

2 Materials and methods

2.1 Research design

This research employs a controlled experimental approach to investigate the impact of light exposure settings in DLP on the mechanical, thermal, and microstructural properties of sintered alumina parts. The study was intentionally designed to evaluate the full process–structure–property relationship of ceramic components produced via additive manufacturing.

To ensure meaningful and reproducible comparisons, sample geometries were selected specifically matched to the characterization methods used. Cylindrical samples were ideal for porosity and density evaluations via the Archimedes method, due to their simple volume and consistent surface contact in immersion tests. Cubic samples, with their flat and measurable surfaces, were better suited for assessing linear and volumetric shrinkage after sintering.

Bars were designed for mechanical testing to assess the structural reliability of the printed ceramics. Three-point bending tests were conducted to evaluate flexural strength and Young's modulus, and the Poisson's ratio of the sintered alumina was estimated from the literature. These tests were chosen because they effectively characterize how brittle materials like alumina respond under loading, offering critical insights into the material's elastic and failure behavior, particularly about printing parameters such as exposure energy and curing depth.

To complete the performance evaluation, the study also included thermal conductivity testing to assess how effectively the sintered alumina samples transfer heat. The test was performed on cylindrical-shaped components that exposed a high base area for heat exchange.

By integrating thermal testing alongside mechanical and structural evaluations, the study aims to provide a comprehensive understanding of how DLP processing influences both the mechanical performance and thermal efficiency of alumina ceramics.

2.2 Ceramic Printing Slurry

The alumina parts were fabricated using a commercial ceramic slurry, AdmaPrint A130, developed by Admatec Europe BV (Alkmaar, Netherlands), that is compatible with the used machine, which was Admaflex 130 Entry (Admatec Europe BV, Alkmaar, Netherlands). This UV-curable formulation contains high-purity alumina (Al_2O_3) particles suspended in a photosensitive resin. It was selected due to its high solid content, excellent dispersion, and compatibility with DLP-based printers. These characteristics made it ideal for producing detailed and dimensionally accurate ceramic components. (Fig. 14).

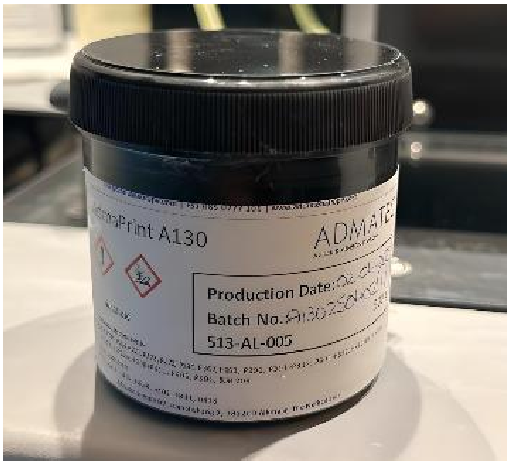

Figure 14. AdmaPrint A130 container

To ensure the correct dispersion of ceramic phase in the suspension, especially after a long storage time, the ceramic slurry was homogenized using a THINKY planetary vacuum mixer 310P (Tokyo, Japan, Figure 15). The resin container was placed in the mixing chamber, carefully balancing materials weight, and the selected parameters for mixing were: 2000 rpm for 120s.

Figure 15. The THINKY Planetary Vacuum Mixer interface shows set parameters (time, speed, and vacuum) for homogenizing ceramic slurry before 3D printing

2.3 DLP printing of ceramic slurry

2.3.1 CAD design

Based on test procedures requirements, different geometries were fabricated: cuboids for evaluating linear and volumetric shrinkage; cylinders for Archimedean density evaluation, as well as for thermal conductivity measurement; bars for mechanical tests. Below is a table that sums up the geometrical characteristics for each type of fabricated sample. (Table 5)

Table 5. Sample Types, Dimensions, and Experimental Applications

Sample Type	Dimensions (mm)	Geometry Description	Application Focus
Cubic samples	15 (L) × 5 (W) × 10 (H)	Baseplate extended 1 mm on all sides (17×7 mm footprint); central 0.5 mm venting channel	Shrinkage evaluation, dimensional change analysis
Cylindrical samples	Ø 10 × 10 (H)	Baseplate with four radial channels (1 mm × 7 mm) arranged in a cross layout	Density and porosity evaluation (Archimedes test)
Bar samples (mechanical)	30 (L) × 4 (W) × 3 (H)	Standard bar geometry per ASTM C1161	Mechanical testing (flexural strength, Young's modulus)
Disc samples (thermal)	Ø 49 × 2 (H)	Flat disc geometry	Thermal conductivity evaluation (GHFM-01 test)

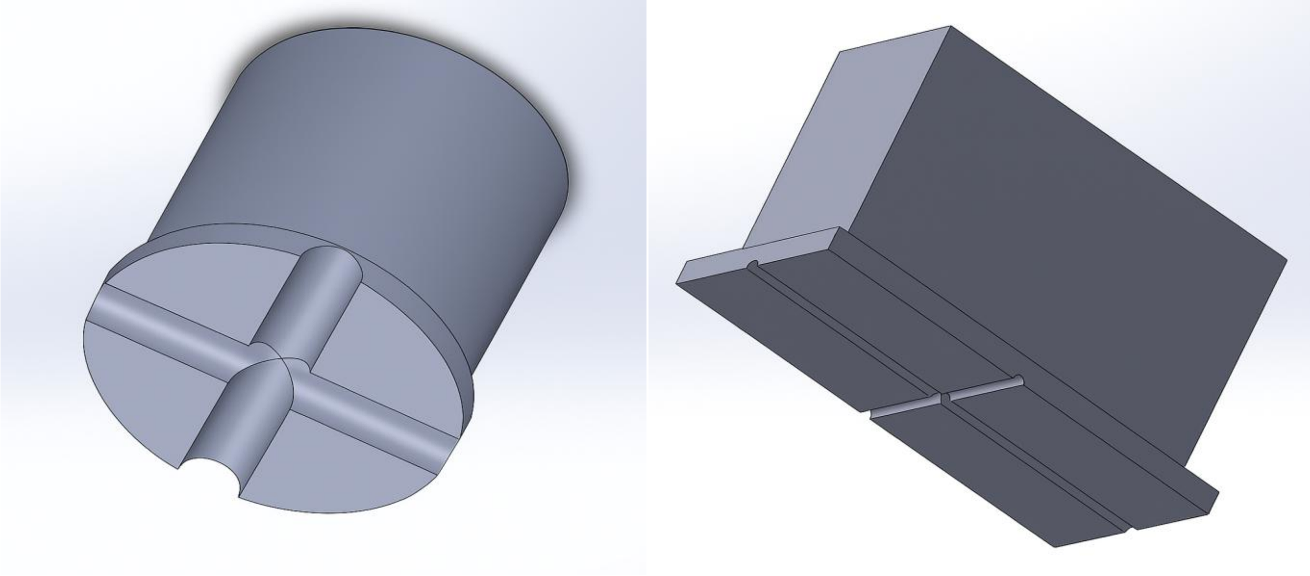

Figure 16. CAD renderings of the STL files used to design the baseplate configurations for cylindrical (left) and cubic (right) ceramic samples

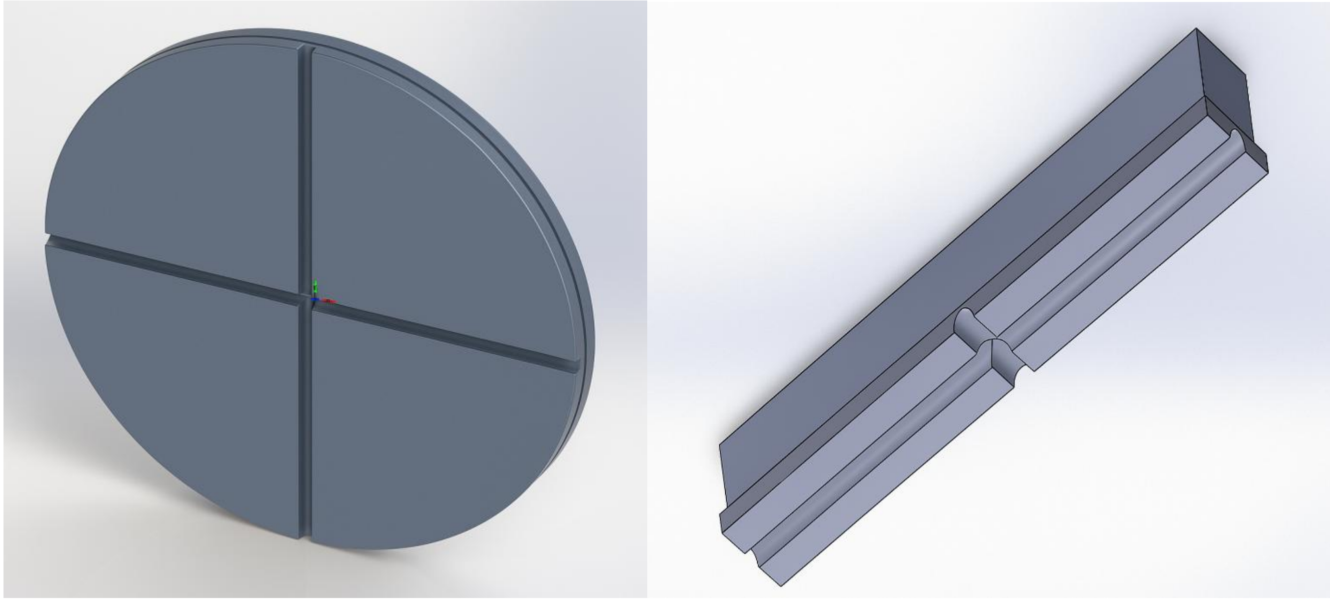

Figure 17. STL renderings of the disc-shaped sample for thermal testing (left) and the bar-shaped sample for mechanical testing (right)

The geometries described were designed using SolidWorks 2024 (Student Version) and exported as. STL files, suitable for 3D printing. STL files of all geometries included an additional baseplate and custom venting feature, which were embedded into baseplates, as required by the used DLP printer. This digital preparation enabled precise control over slicing, baseplate layout, and exposure settings within the Admaflex software.

2.3.2 Pre-printing controls: DoC test

To determine the optimal exposure conditions for photopolymerizing the alumina slurry, a Depth of Cure calibration test was conducted using the Admaflex 130 Entry printer. A uniform disc of AdmaPrint A130 slurry was deposited onto a foil-covered glass substrate and exposed using the printer's "Test Projector" function. LED power, exposure duration, and pattern were configured through the printer's manual interface. Following exposure, the uncured slurry was removed with a lint-free tissue, and the thickness of the cured region was measured using a digital micrometer, which was carefully zeroed against the foil baseline before each reading.

It's important to note that curing behavior can be influenced by environmental conditions, such as temperature and humidity. These factors may alter resin sensitivity and the depth of light penetration, making pre-print DoC testing an essential part of the preparation process. By determining optimal exposure settings through calibration, the print process becomes more reliable and consistent, minimizing errors and boosting overall print quality.

The procedure was repeated for various exposure settings to evaluate the relationship between curing depth and printing parameters. Based on the results, target curing depths were determined for two-layer thicknesses commonly used during slicing: approximately 90 µm for 30 µm layers, and 150 µm for 50 µm layers. These optimal DoC values were directly applied to define the slicing settings in Admaflex software.

Once DoC calibration was complete, STL models were imported into the Admaflex software (v1.25.1) for printing preparation. Each model was manually oriented using the software's rotation controls to improve build quality and ensure stable stacking. Shrinkage compensation was applied based on expected material behavior during sintering, using scale factors adjusted in the XY and Z axes.

2.3.3 Material shaping: DLP printing

Following slicing and model orientation, the 3D printing jobs were configured using the printer's user interface, which offers full control over all critical process parameters. For this study, two-layer thickness settings—30 µm and 50 µm—were selected to evaluate their influence on resolution and microstructural integrity. These values fall within the recommended slice thickness range for alumina (30–50 µm), as specified by Admatec for their Admaflex ceramic printing systems. Selecting both ends of this range enabled a meaningful comparison between high-resolution printing (30 µm), which enhances surface finish and interlayer bonding, and faster, coarser printing (50 µm), which reduces build time but may compromise detail. This strategy supports a comprehensive understanding of how exposure thickness affects the final part quality in terms of mechanical, dimensional, and visual properties.

The printing was performed on a ceramic-compatible DLP printer that supports a build volume of 102 × 64 × 400 mm³ and resolution down to 40 µm in the XY-plane. Slicing and print parameters were configured using proprietary software, which offered adjustable settings for LED power, exposure duration, and layer-specific configurations. (Fig.18)

Figure 18. The Admaflex 130 Entry system is used for ceramic sample fabrication

To ensure high-resolution output and stable green parts, each print job was segmented into four exposure regions, each with customized parameters:

- Base Layer Initialization:

The first slice (slice 0) was exposed for an extended duration (typically 15,000–25,000 ms) to ensure strong adhesion between the initial layer and the build platform. This exposure was repeated across the first few layers to establish a stable foundation.

- Baseplate Formation:

The following slices (1–32 for 30 µm and 1–19 for 50 µm) formed the sample baseplate. Exposure settings were derived from prior DoC calibration to guarantee sufficient polymerization and interlayer bonding. Additional motion delays and adjusted platform travel distances were introduced to reduce mechanical stress during this critical phase.

- Breakaway Interface:

To facilitate clean removal of the part from the baseplate, two intermediate slices (e.g., slices 33–34) were subjected to over- and under-exposure, deliberately creating a controlled weak zone for simplified post-print separation.

- Model Construction:

The remaining slices defined the actual geometry of the printed part. Exposure settings for this phase followed the standard parameters identified during the DoC calibration, enabling uniform curing, accurate feature reproduction, and robust green part strength.

Printing: delay before exposure
"cubic30"
Size: 57.0 × 37.0 × 11.0 mm, 10.431 cm³
Layer: 38 / 370 (10%)   Time left: 5h 28m 27s / 6h 11m 36s
Remaining foil: 88 to 103 m   Humidity: 33.1 %   Temperature: 27.1 °C

5h 28m

Pixel value part 1–12	1 000 %
Exposure time part 1–12	15 000 ms
Slice 1–20	
Thickness	30 µm
Repeat	1 ×
Up/down distance	15 000 µm
Exposure time part 1–12	5 000 ms
Slice 21–32	
Up/down speed	2 000 µm/s
Up/down acceleration	2 000 µm/s²
Slow down distance	400 µm
Slice 33	
Transport acceleration	5 000 µm/s²
Up/down distance	10 000 µm
Exposure time part 1–12	50 000 ms
Slice 34	
Thickness	60 µm
Up/down distance	5 000 µm
Exposure time part 1–12	5 000 ms
Slice 35–367	
Thickness	30 µm

Current slice: 35

Figure 19. Status screen showing layer progression, remaining time, and environmental conditions during printing

Upon completion, the printed parts were removed and processed for cleaning and sintering, as described in the subsequent steps.

2.3.4 Post-processing of printed samples

- Solvent Cleaning:

After printing, the green ceramic components still retained residual uncured resin, especially in narrow channels and small cavities. To ensure clean and defect-free sintering, the parts were soaked in Tri-propylene Glycol Monomethyl Ether (TPM), from 3D-Basics. This solvent was selected for its high resin solubility and safe interaction with the fragile green body. Its low volatility and deep penetration made it ideal for removing uncured material without inducing surface damage. This essential step laid the groundwork for the subsequent ultrasonic cleaning process. To improve the efficiency of resin removal, the samples were also subjected to ultrasonic cleaning using the CP104 ultrasonic cleaner (CEIA, Arezzo, Italy) (Fig.20).

Figure 20. CP104 ultrasonic cleaner during post-processing

- Debinding and sintering:

After the cleaning process, the green ceramic parts were transferred to a bottom-loading high-temperature furnace (Admatec 450-CH-400), specifically configured for integrated debinding and sintering operations. The furnace is equipped with a programmable controller that enables precise control of multi-stage heating and cooling, reaching peak temperatures of up to 1625 °C. (Fig. 21).

Figure 21. Integrated debinding and sintering furnace for alumina parts

The debinding and sintering process followed the standard profile optimized for alumina, which is summarized in Table 6. This thermal cycle includes controlled ramp rates, dwell times, and critical transitions necessary to remove the organic matrix and achieve full ceramic densification.

Table 6. Combined debinding and sintering profile for alumina parts

Stage No.	Temperature (°C)	Rate (°C/h)	Time (hours)
1	RT – 150	25 ↑	5.0
2	150	Dwell	0.5
3	150 – 325	8 ↑	21.5
4	325	Dwell	1.5
5	325 – 420	8 ↑	12.0
6	420	Dwell	1.0
7	420 – 600*	12 ↑	15.0
8	600 – 1000	60 ↑	6.5
9	1000	Dwell	1.0
10	1000 – 1625	100 ↑	6.25
11	1625	Dwell	3.0
12	1625 – RT	200 ↓	±8.0

*RT: Room temperature; ↑ Heating; ↓ Cooling
*The transition at Stage 7 is considered critical for binder burnout.

2.4 Sample characterization

2.4.1 Dimensional Measurement

Immediately after printing, green-body specimens were measured using a vernier caliper with 0.05 mm resolution. These values were later used to calculate linear and volumetric shrinkage after sintering. (Fig. 22)

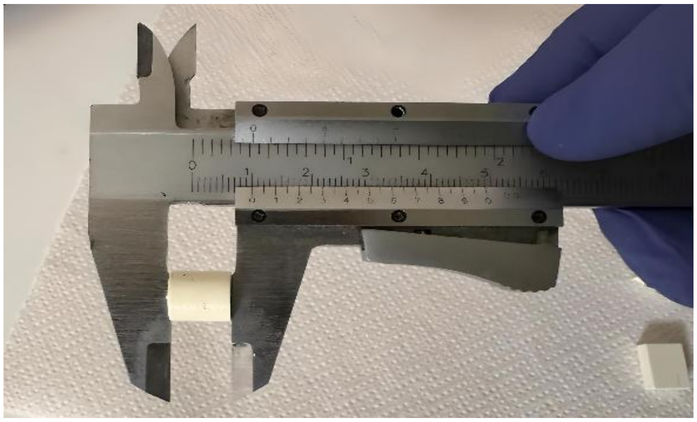

Figure 22. Caliper-based diameter measurement

After sintering**,** shrinkage analysis was performed on cubic samples. It aimed to quantify the dimensional changes occurring during sintering. This is important for controlling final dimensions and understanding densification behavior and the risk of defect formation (79), (80) .

Dimensional measurements were taken before and after sintering using a precision caliper. Linear shrinkage was calculated in length, width, and height directions, and volumetric shrinkage was determined based on changes in overall sample volume.

Equations used:

Linear Shrinkage (%)

$$\text{Linear Shrinkage \%} = \frac{L_{\text{after}} - L_{\text{before}}}{L_{\text{before}}} \times 100 \qquad \textbf{(1)}$$

Volumetric Shrinkage (%)

$$\text{Volumetric Shrinkage \%} = \left(1 - \frac{L_{after} \times W_{after} \times H_{after}}{L_{before} W_{before} \times H_{before}} \right) \times 100 \qquad \textbf{(2)}$$

Where:

$L_{after}, W_{after}, H_{after} =$ Dimensions before sintering (mm)

$L_{before}, W_{before}, H_{before} =$ Dimensions after sintering (mm)

These calculations provided a clear and quantitative understanding of how the samples densified and retained their dimensions during sintering, offering a solid basis for evaluating the overall effectiveness of the printing and thermal post-processing parameters.

2.4.2 Density measurement

To evaluate densification behavior, microstructural consistency, and the overall success of the additive manufacturing and sintering workflow, porosity and density measurements were conducted on cylindrical specimens.

Porosity and density evaluation were carried out using the Archimedes method (81) , a widely adopted technique for sintered ceramics such as alumina. It relies on the buoyancy principle first described by Archimedes, which states that an object submerged in a fluid experiences a buoyant force equal to the weight of the displaced fluid (82,83) .

By ASTM C773-88 (84), this method was applied to each sintered cylindrical sample to determine both geometric and apparent densities. The analysis involved three key mass measurements: the dry mass (in air), immersed mass (submerged in water), and saturated mass (after immersion and surface drying).

To ensure full pore saturation, each sample was submerged in water in a petri dish and degassed using a Pfeiffer vacuum pump. The appearance of air bubbles confirmed the removal of trapped air. Following this, immersed and saturated masses were recorded, and porosity calculations were performed using buoyancy-based equations. The theoretical density of alumina, based on the manufacturer's suggestion, was taken as 3.9 g/cm³, and all measurements were conducted at 26.1 °C (ρ_water = 0.997 g/cm³).

Equations used:

Apparent Density:

$$\rho_{\text{apparent}} = \frac{W_{\text{air}}}{W_{\text{wet}} - W_{\text{water}}} \times \rho_{\text{water}} \qquad \textbf{(3)}$$

Real Density:

$$\rho_{\text{real}} = \frac{W_{\text{air}}}{W_{\text{air}} - W_{\text{water}}} \times \rho_{\text{water}} \qquad \textbf{(4)}$$

Open Porosity (%):

$$\text{Open Porosity \%} = \frac{W_{\text{wet}} - W_{\text{air}}}{W_{\text{wet}} - W_{\text{water}}} \times 100 \qquad \textbf{(5)}$$

Closed Porosity (%):

$$\text{Closed Porosity \%} = \frac{\rho_{\text{theoretical}} - \rho_{\text{real}}}{\rho_{\text{theoretical}}} \times 100 \qquad \textbf{(6)}$$

Total Porosity (%):

$$\text{Total Porosity \%} = \frac{\rho_{\text{theoretical}} - \rho_{\text{apparent}}}{\rho_{\text{theoretical}}} \times 100 \qquad \textbf{(7)}$$

Where:

W_{air} = Mass of the sample in air [g]

W_{wet} = Wet mass of the sample [g]

W_{water} = Mass of the sample when submerged in water [g]

ρ_{water} = Density of water $((0.997\frac{g}{cm^3})$ at 26.1°C)

$\rho_{theoretical}$ = theoretical density of Alumina ($3.9\ \frac{g}{cm^3}$)

$\rho_{apparent}$ = Apparent density of the material ($\frac{g}{cm^3}$)

ρ_{real} = Real density of the material ($\frac{g}{cm^3}$)

2.4.3 Mechanical Testing Samples

For mechanical testing, rectangular bar-shaped samples were designed following ASTM C1161-18 guidelines (85) for a three-point bending test of advanced ceramics. The CAD design defined the nominal dimensions as 30 mm in length, 4 mm in width, and 3 mm in height. The three-point bending method provided values for both flexural strength and Young's modulus.

These values were selected to ensure compatibility with standard support spans and to promote fracture at the sample midpoint. The test geometry was chosen to reflect the brittle nature of ceramics and ensure well-distributed stress under central loading. Dimensional uniformity was maintained across all samples during the printing phase. (Fig.23)

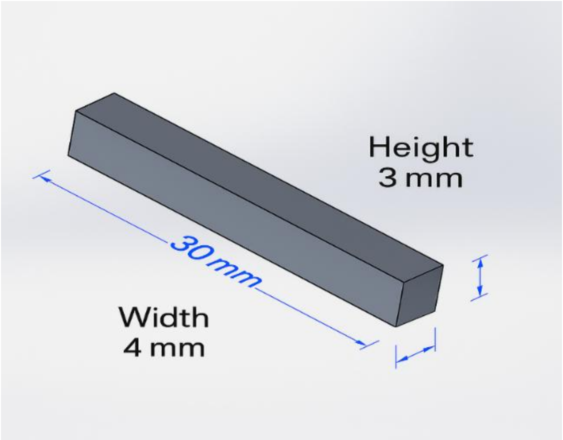

Figure 23. CAD model of the three-point bending test bar

Mechanical tests in this study were performed using the Instron 2710-112 (Norwood, Massachusetts, USA) screw side-action grip. It has a capacity of 500 N and a U-shaped aluminum body and is specifically designed for the static mechanical characterization of various material types, including ceramics, plastics, thin sheets, metals, and textiles.

A 14 mm support span was selected based on the geometry of the test fixture. Rectangular alumina specimens were positioned horizontally on the support grips (Fig. 24), and a central load was applied at a constant rate until fracture occurred.

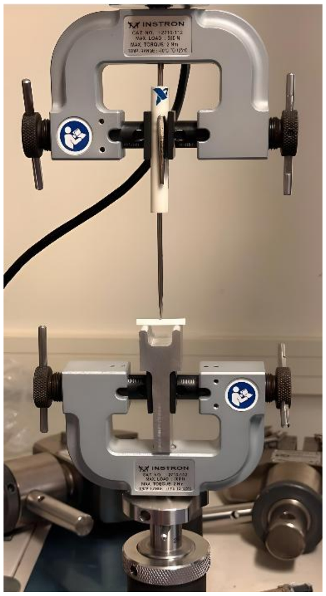

Figure 24. Three-point bending configuration showing bar sample underload using standard INSTRON fixture

This loading setup induced tensile stress on the bottom surface of the sample, with the highest stress concentration located at mid-span. During testing, the force–displacement curve was recorded. The maximum force (F) at fracture was used to calculate flexural strength, while the initial linear portion of the curve, corresponding to the elastic regime, was analyzed to determine the slope (m). This slope was used to estimate the Young’s modulus (E) of the material (Fig.25).

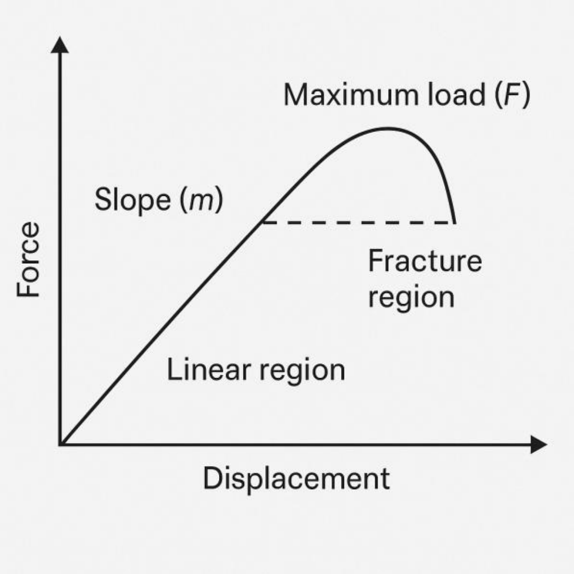

Figure 25. Force–displacement curve for flexural test indicating linear and fracture regions

The flexural strength σ_f was calculated using:

$$\sigma_f = \frac{3FL}{2bd^2} \qquad \textbf{(8)}$$

Where:

Maximum load at fracture (N)

Support span = (L=14 mm)

Sample width = (b=4 mm)

Sample thickness = (d=3 mm)

Young's modulus was calculated from the slope of the initial linear (elastic) region of the force–displacement curve, using the following formula:

$$E = \frac{L^3 m}{4bd^3} \qquad \textbf{(9)}$$

Where:

Support span (L=14 mm)

Slope of the elastic region (m=N/mm)

Width of the specimen (b=4 mm)

Thickness of the specimen (d=3 mm)

Additionally, the Poisson's ratio (ν) of sintered alumina was assumed based on values reported in literature, typically ranging from 0.21 to 0.25, with $\nu \approx 0.22$ adopted as a representative value for dense, high-purity alumina ceramics. (86)(87)

2.4.4 Thermal Testing Samples

Thermal characterization was performed using the GHFM-01 Guarded Heat Flow Meter (Hanwell, Canada), a high-precision instrument tailored for steady-state measurement of thermal resistance and conductivity. Fully compliant with ASTM E1530-19 (88)The device includes integrated temperature-controlled plates, a guard ring to minimize edge heat losses, and an automated clamping system capable of adjusting thickness and pressure for accurate readings. A separate liquid chiller set at 10 °C was employed to maintain consistent thermal conditions during the test. Certified reference standards such as Pyrex 7740 ½', stainless steel ¼', and 1, which were used for calibrating testing temperatures (100°C – 150°C, 200°C – 250°C) to ensure reliable and reproducible results. (Fig.26)

Figure 26. GHFM-01 Guarded Heat Flow Meter system for ceramic disc testing

For thermal performance evaluation, disc-shaped ceramic specimens were designed with a CAD diameter of 50 mm and a thickness of 2 mm. They maintained proper alignment and surface contact during testing. (Fig. 27)

Before testing, thermal contact paste was applied to both surfaces to reduce contact resistance. The instrument automatically measured thickness and applied clamping force. Thermal resistance R_s and thermal conductivity λ were calculated after the system reached a steady state.

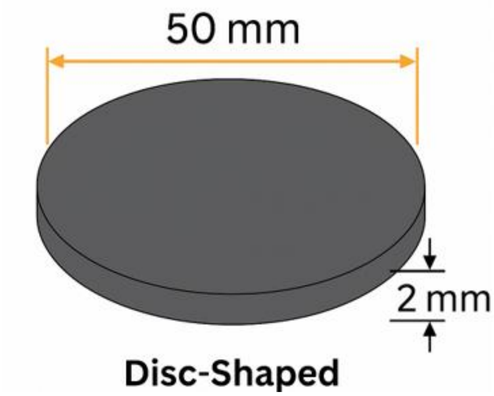

Figure 27. Drawing of a disc-shaped ceramic sample designed for thermal conductivity testing.

2.5 Numerical Simulation of a Ceramic Thermal Dissipator

In the final phase of this study, a ceramic thermal dissipator was designed and numerically simulated to evaluate the thermal and mechanical performance of sintered alumina in practical thermal management applications. The objective was to understand how well alumina can function under conditions of localized heating and geometric constraints, as typically encountered in compact power electronics or microelectronic modules.

The simulated component consisted of a rectangular alumina plate with a repeating hexagonal cut-out pattern, intended to reduce weight and enhance thermal interaction with the surrounding environment. Additionally, four vertical cylindrical holes were included to allow the flow of cooling water directly through the ceramic body, simulating active internal convection in an integrated system.

The 3D geometry was created in SolidWorks 2024 and exported as a STEP file for Multiphysics analysis. The final dimensions of the component were 19.57 mm (width) × 27.8 mm (length) × 1.4 mm (thickness). To replicate realistic thermal system behavior, two additional domains were included in the simulation setup:

- A copper plate was modeled beneath the ceramic part to serve as the heat source, representing a real electronic element such as a printed circuit board or embedded resistor.

- A fluid domain filled with water was added to represent the cooling medium. The water flows through the cylindrical holes in the alumina, facilitating heat removal via internal convection. (Fig.28)

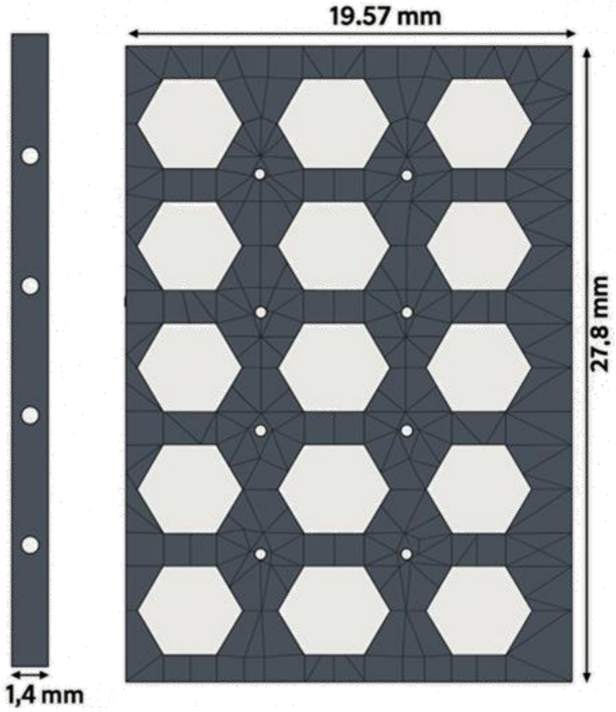

Figure 28. Thermal Dissipator CAD Model; Front and side views of the DLP-printed thermal dissipator with hexagonal cut-outs

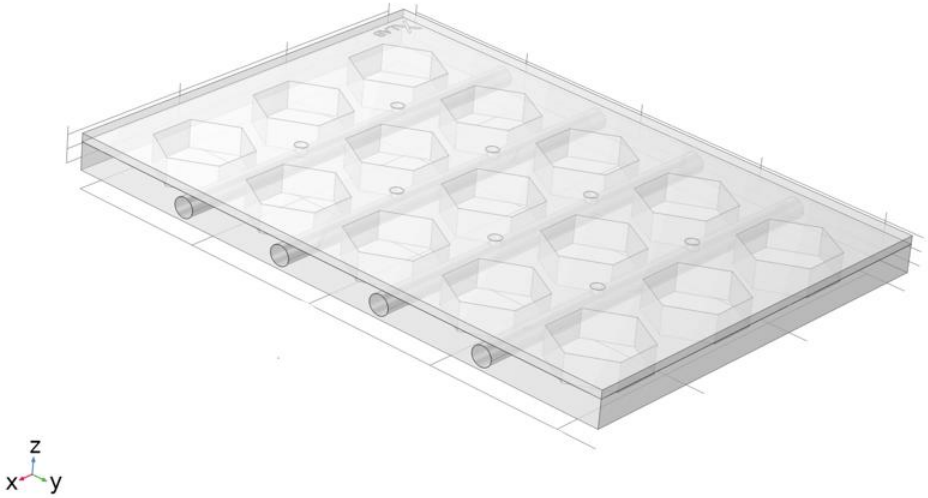

Figure 29. Geometric model of the alumina thermal dissipator imported into COMSOL Multiphysics.

The full assembly was imported into COMSOL Multiphysics 6.3, where the automatic mesh generator was used to discretize the geometry, and simulations were conducted under steady-state conditions.

The automatic mashing ensured efficient resolution in critical areas—such as the hexagonal perforations and internal channels—without excessive computational load, maintaining a balance between accuracy and performance.

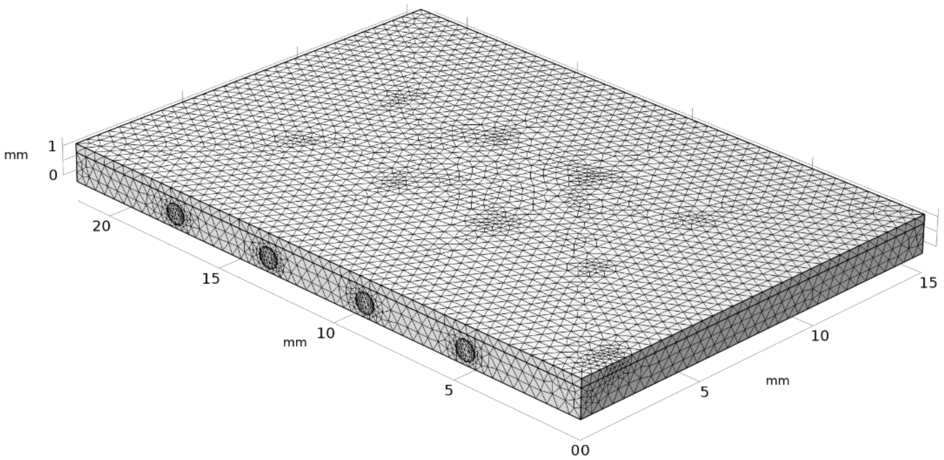

Figure 30. Finite element mesh of the simulated alumina thermal dissipator generated using COMSOL's automatic meshing algorithm. The mesh captures the complex geometry of the hexagonal cut-outs and cylindrical fluid channels with refined local discretization for accurate thermal and mechanical coupling analysis.

A 10 W heat source was applied to the copper plate. This mimicked the Joule heating effect typical of powered circuits or embedded resistive elements. Instead of modeling voltage or current input, the thermal power was directly prescribed, simplifying the analysis while maintaining physical realism. The outer edges of the alumina plate were mechanically constrained, mimicking how ceramic components are mounted inside thermal modules using screws or brackets. These constraints prevented displacement in all directions, enabling evaluation of realistic thermal expansion effects under boundary restrictions.

The overall simulation allowed simultaneous analysis of:

- Thermal field evolution across the copper, alumina, and fluid regions
- Mechanical deformation and stress patterns induced by internal heating and fixed mounting

These modules were integrated to allow the fluid temperature to evolve in response to internal heating from the copper, while thermal gradients and fluid pressure drove mechanical deformations in the alumina.

The simulation was conducted with several assumptions and configurations, implemented to realistically capture the coupled thermal–mechanical behavior of the ceramic thermal dissipator under steady-state operating conditions.

The fluid flow inside the vertical holes of the alumina was modeled using a laminar flow regime (89), which is appropriate for low Reynolds number scenarios in microscale internal channels. COMSOL's laminar flow module solved the Navier–Stokes equations, accordingly, ensuring accurate flow behavior within the constrained geometry.

Because the analysis was performed in steady-state mode, initial conditions for fluid velocity and pressure were both set to zero. These values are only relevant in transient analyses and were omitted here, assuming the system had already reached thermal and flow equilibrium before analysis began.

At the fluid–solid interfaces, no-slip boundary conditions were applied. This widely accepted assumption ensures that the fluid velocity is zero at the walls and is commonly used for internal channel flow in both experimental and numerical setups.

Convective cooling was simulated by introducing water flow through the four vertical holes in the ceramic body. To drive the internal convection, a flow rate of 0.1 l/min at 25 °C was imposed at the inlet, while the outlet was defined as a zero-pressure boundary condition and no fixed temperature condition. This setup allowed COMSOL to solve for the internal pressure field required to sustain the defined flow rate, without needing explicit pressure inputs. This also allowed the simulation to calculate the thermal exchange outcome as a function of internal heat transfer between copper, ceramic, and fluid.

The full model was divided into complementary solid and fluid domains:

- The solid domains included the alumina ceramic and copper plate, where heat conduction and thermal expansion were modeled.
- The fluid domain consisted of water within the four vertical cylindrical channels embedded in the ceramic structure.

This domain separation allowed for accurate Multiphysics coupling of heat conduction in solids and convection in fluids.

The initial temperature for all simulation domains was set to 25 °C, reflecting ambient operating conditions before activation of the copper heat source. Since the simulation was steady state, this value was used only to initialize the solver, as temperature evolution was solved based on internal heating.

All external boundaries—except for the copper–alumina interface, the alumina–fluid interface, and the fluid inlet and outlet—were modeled as thermally insulated. These settings ensured that heat transfer occurred only at physically meaningful surfaces, focusing the simulation on internal system behavior.

Lastly, ambient air was deliberately excluded from the model. Due to its low thermal conductivity and negligible heat exchange effect in enclosed systems, air was not considered a significant contributor. This allowed the simulation to focus entirely on heat exchange between the three core domains: copper (source), alumina (conductor/insulator), and water (coolant).

For mechanical analysis, only the alumina plate was included. The copper and water domains were omitted from the mechanical simulation because copper is highly ductile and typically not rigidly attached to ceramics in real systems, while water does not form fixed mechanical interfaces. In actual applications, the copper plate typically rests on top of the ceramic and may be loosely placed or screwed down, but it is not rigidly glued. Including it in the mechanical model would imply unrealistic stiffness and constraint transmission, which could distort the results.

Mechanical constraints were applied exclusively to the outer edges of the alumina. This strategy avoided over-constraining the model and enabled the simulation to realistically capture bending, thermal expansion, and stress localization across the plate.

In addition to thermally induced expansion, the influence of hydraulic pressure from the internal water flow was incorporated into the mechanical analysis. This addition provided insight into whether internal pressure, especially under high laminar flow conditions, could generate localized stresses or even contribute to cracking near the fluid channels.

3 Results

3.1 Exposure Calibration of Green-Body Parts

DoC calibration test was performed to optimize the exposure parameters for two selected layer thicknesses: 30 µm and 50 µm. As illustrated in Figure 31, the target DoC values were approximately three times the nominal layer thickness, i.e., 90 µm for 30 µm layers and 150 µm for 50 µm layers, aligning with established best practices for DLP photopolymerization.

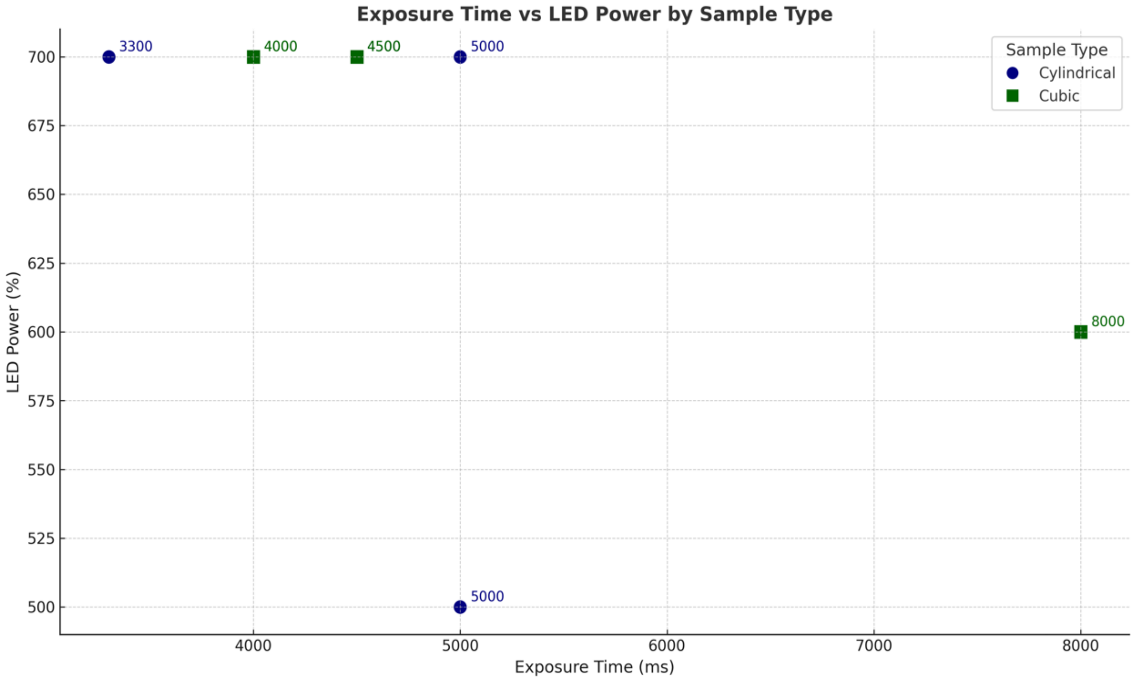

Figure 31. Relationship between exposure time and LED power for cylindrical and cubic samples.

The exposure settings obtained from this calibration were used in the slicing phase via the Admaflex software. For each geometry, the slicing process converted the 3D CAD model into 2D image layers, projecting each slice using optimized exposure times for accurate polymerization and reduced overcuring. The final slicing configurations are shown in Figure 32.

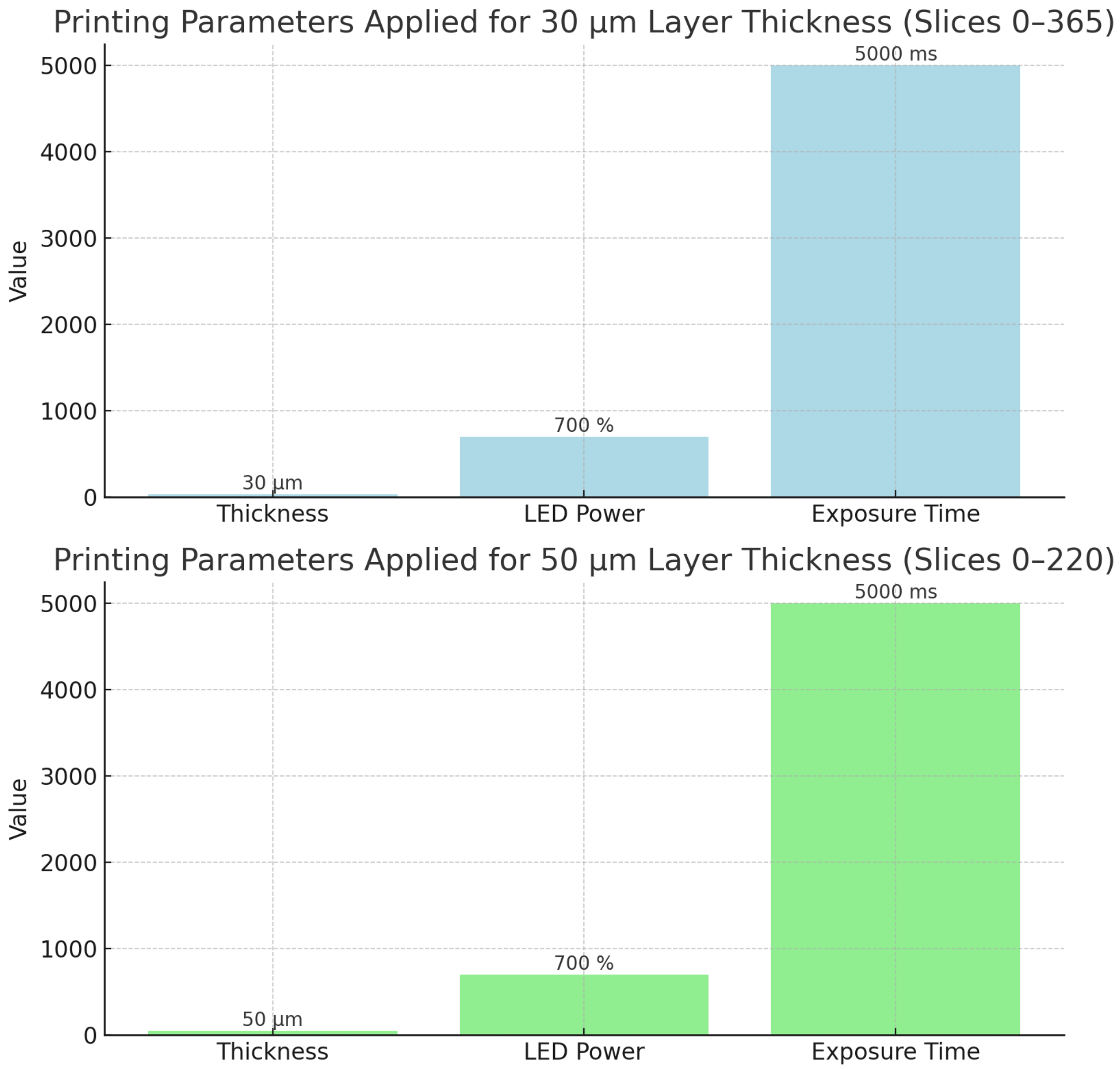

Figure 32. Printing parameters applied for 30 µm and 50 µm layer thicknesses, showing the selected values of layer thickness, LED power, and exposure time during the slicing process for each configuration (Slices 0–365 for 30 µm and Slices 0–220 for 50 µm).

3.2 Dimensional Accuracy of Green-Body Samples

Following the printing process, dimensional measurements were carried out on a total of 60 green-body samples to assess the fidelity of the printed parts relative to their digital specifications. Measurements were taken using a precision vernier caliper (0.05 mm resolution) immediately after printing.

The cylindrical parts were printed using a 50 µm layer thickness, with 220 total slices. All specimens exhibited excellent reproducibility, measuring exactly 10.00 mm in height and 10.00 mm in diameter, with no deviation observed across the four job batches. (Table 7)

Table 7. Dimensional Characteristics of Cylindrical Green-Body Samples

Parameter	Value
Number of Samples	30
Number of Print Jobs	4
Designed Height (mm)	10.00
Designed Diameter (mm)	10.00
Layer Thickness (µm)	50
Number of Slices	220
Measured Variation	None observed
Measurement Tool	Vernier Caliper (0.05 mm res.)

For cubic samples, dimensional variation in height was intentionally introduced to investigate the influence of slicing strategy. All samples shared the same length (15 mm) and width (5 mm), while the height varied across the three job batches:

- Job 1: 8 mm height, 300 slices at 30 µm
- Job 2: 10 mm height, 367 slices at 30 µm
- Job 3: 10 mm height, 220 slices at 50 µm

These controlled variations aimed to evaluate the correlation between slicing parameters and vertical print accuracy. All printed samples showed tight dimensional grouping, indicating a high level of process control.

Table 8. Dimensional Characteristics of Cubic Green-Body Samples

Parameter	Value
Number of Samples	30
Number of Print Jobs	3
Designed Length (mm)	15
Designed Width (mm)	5
Designed Heights (mm)	8, 9.9, 10
Layer Thickness (µm)	30 and 50
Number of Slices	220, 300, 367
Job Variations	Job 1: 8 mm, 300 slices, 30 µm
	Job 2: 10 mm, 367 slices, 30 µm
	Job 3: 10 mm, 220 slices, 50 µm
Measurement Tool	Vernier Caliper (0.05 mm res.)

3.2.1 Porosity and Density Analysis via Archimedes' Method

To quantify the porosity and density of the sintered ceramic parts, the Archimedes method was employed following the ASTM C773-88 standard (84) . The samples analyzed were cylindrical and had undergone full sintering after printing with a 50 µm layer thickness.

Results are summarized in Table 4, including statistical descriptors such as mean and standard deviation for each measured and derived parameter. (Table 9).

Table 9. Summary of Porosity and Density Measurements for Sintered Cylindrical Samples

Parameter	Mean Value	Standard Deviation
Closed Porosity (%)	28.69 %	5.77 %
Total Porosity (%)	29.61 %	5.72 %
Open Porosity (%)	1.25 %	0.88 %
Real Density (g/cm^3)	2.85	0.23
Apparent Density (g/cm^3)	2.83	0.22

Wet Mass (g)	1.35	0.01
Submerged Mass (in Water) (g)	0.873	0.04
Dry Mass (in Air) (g)	1.34	0.01

The average total porosity of 29.61% reflects the relatively high void content associated with partially densified ceramic structures produced via DLP, which is expected when using non-pressurized sintering. Notably, closed porosity constituted most of this value (28.69%), while open porosity remained low (1.25%), indicating that the internal pores were effectively sealed during thermal processing.

The measured real density (2.85 g/cm^3) and apparent density (2.83 g/cm^3) are slightly below the theoretical density of fully dense alumina (3.9 g/cm^3), confirming the presence of retained porosity. However, the proximity of these two values suggests that most porosity is internal and not surface-connected, which aligns with expectations for well-sintered ceramic. It should be noted that these results may also be influenced by measurement uncertainty, particularly the resolution of the precision scale used and environmental factors. Additionally, the method of support measurement may have further contributed to minor deviations.

The standard deviations observed in porosity (±5.7%) and density (±0.22–0.23 g/cm^3) were within acceptable ranges, indicating a high level of repeatability in both measurement and process outcomes. In particular, the open porosity variation of only ±0.88% supports the conclusion that the vacuum degassing and sintering steps were consistently executed.

Low variability in dry and wet mass (±0.01 g) further strengthens the reliability of the Archimedes-based measurements. These results confirm that the combination of exposure parameters, slurry formulation, and sintering protocol yielded uniform and reproducible ceramic microstructures across all samples.

3.2.2 Shrinkage Analysis of Cubic Samples Before and After Sintering

To complement internal porosity assessment, shrinkage measurements were conducted on the cubic samples by comparing their geometrical dimensions before and after sintering in all three principal direction -length (X), width (Y), and height (Z).

The results are summarized in Table 10, reporting both mean dimensional values and standard deviations. Shrinkage was computed as the percentage reduction in each axis, and total volumetric shrinkage was derived accordingly.

Table 10. Dimensional Changes and Shrinkage of Cubic Samples Before and After Sintering

Parameter	Average Value	Standard Deviation
Height Before Sintering	9.20 mm	± 0.99 mm
Height After Sintering	6.67 mm	± 0.72 mm
Height Shrinkage (%)	-27.5 %	± 0.66 %
Length Shrinkage (%)	-22.0 %	0 %
Width Shrinkage (%)	-22.0 %	0 %
Volumetric Shrinkage (%)	55.89 %	± 0.40 %

The shrinkage results confirmed a strong densification trend following sintering. Height shrinkage averaged 27.5%, corresponding to the Z-axis. The associated variability (±0.66%) likely reflects differences in initial green-body height across the 8 mm and 10 mm batches, as well as localized variations in vertical thermal gradients during sintering.

Shrinkage in the lateral direction length and width (X and Y axes) was highly consistent, with a uniform reduction of 22.0% and zero standard deviation. This repeatability indicates excellent process control and geometric uniformity in the printed samples.

The overall volumetric shrinkage was calculated to be 55.89%, a value typical for high-purity alumina ceramics processed via non-pressurized sintering. The low standard deviation of ±0.40% further confirms the repeatability and control of the process.

The observed low variability, particularly in the horizontal shrinkage, demonstrates the reliability of the DLP-based printing process in producing dimensionally accurate ceramic components. These results suggest that the combination of carefully calibrated exposure settings, uniform layer deposition, and thermally optimized sintering protocols enabled consistent material shrinkage without inducing structural distortion.

The high-dimensional precision and repeatable contraction across all samples validate the effectiveness of the adopted process parameters in achieving controlled densification. These outcomes support the suitability of the printed alumina parts for advanced technical applications requiring tight geometric tolerances. (Fig. 33,34)

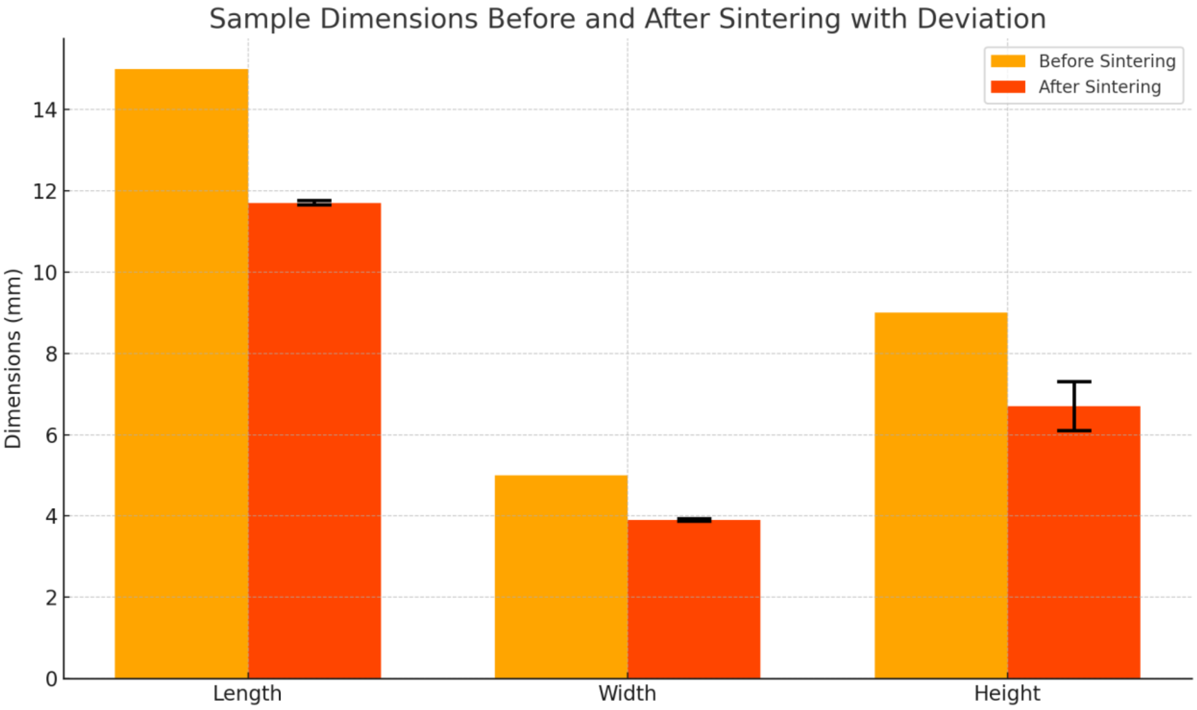

Figure 33. Average linear shrinkage along the height, length, and width of sintered cubic samples, highlighting dimensional contraction due to densification during thermal processing. Standard deviation bars are included to indicate measurement variability across samples.

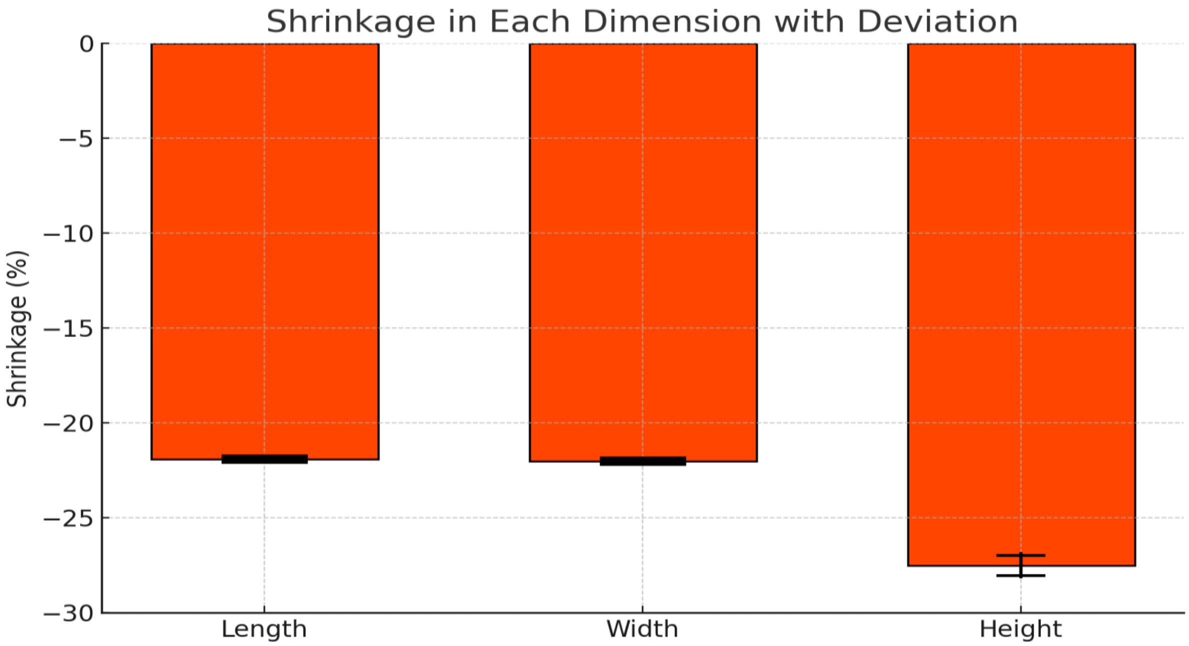

Figure 34. Volumetric shrinkage of cubic samples post-sintering, representing overall dimensional reduction in all three axes, with associated deviations representing measurement variability

3.3 Mechanical Testing of alumina bars

3.3.1 Flexural Strength Evaluation

The mechanical performance of sintered alumina specimens produced by DLP-based additive manufacturing was assessed through three-point bending tests, following the ASTM C1161 (85) standard. Out of 14 printed bar-shaped samples, 10 were selected for mechanical evaluation to ensure statistical consistency and test reliability.

The flexural strength was calculated using the classical bending formula for rectangular beams, as outlined in the Materials and Methods section. The results demonstrated a range of flexural strengths between 206.2 MPa and 247.5 MPa, with a calculated mean of 228.07 MPa and a standard deviation of ±14.35 MPa. The mean maximum load at fracture was recorded as 390.96 N. Figure 33 illustrates the distribution of the flexural strength values across the tested samples.

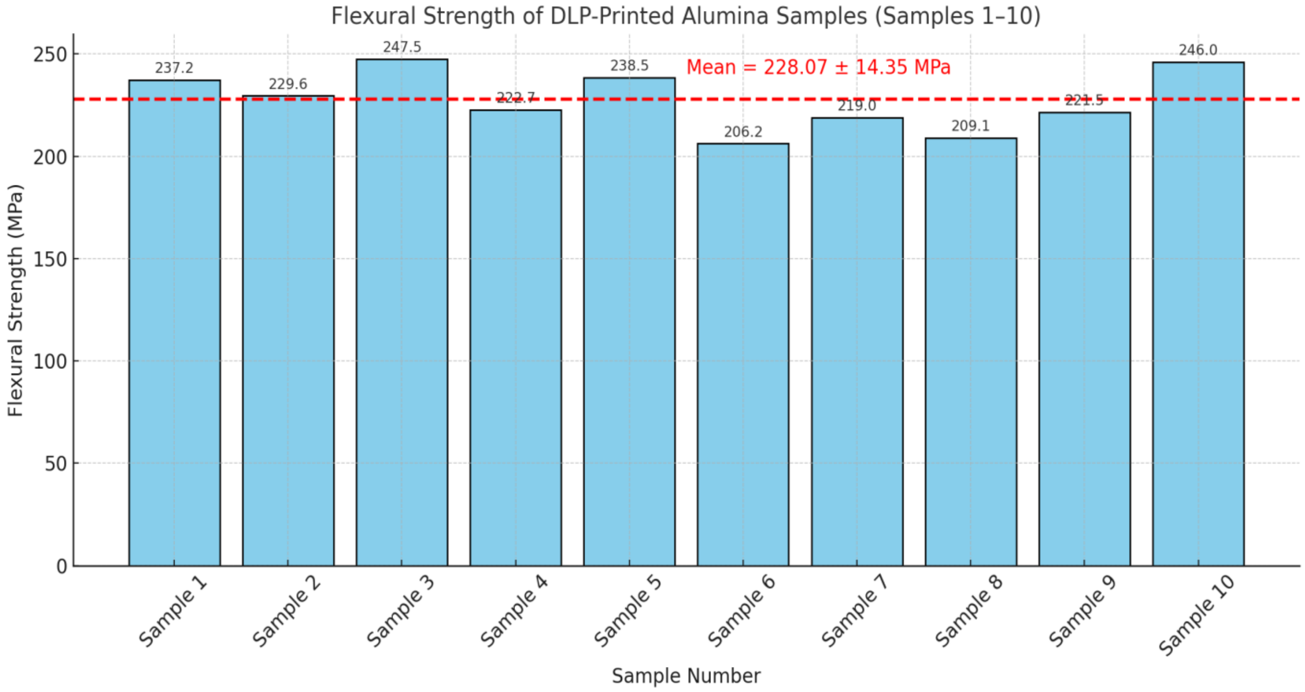

Figure 35. Flexural strength distribution of DLP-printed alumina samples tested via three-point bending

The key experimental parameters and results are summarized in Table 11:

Table 11. Summary of flexural strength testing parameters and outcomes

Parameter	Value	Unit	Notes
Number of Tested Samples	10	–	Selected from 14 total printed bars
Mean Flexural Strength	228.07	MPa	Based on the maximum load at fracture
Strength Standard Deviation	±14.35	MPa	Indicates consistency in fabrication
Mean Maximum Load (F)	390.96	N	Load at fracture
Support Span (L)	14	mm	Fixed by test fixture
Width (b)	4	mm	Measured pre-sintering
Thickness (d)	3	mm	Measured pre-sintering
Testing Machine	INSTRON 2710-112	–	Equipped with a 500 N load cell

Although the measured values fall slightly below the expected range for dense sintered alumina (typically 260–300 MPa), the results remain within the expected domain for ceramic parts with significant porosity (~30%). Table 12 presents a comparison with previously reported values from literature.

Table 12. Comparison of Flexural Strength Values for Alumina Ceramics

Study	Fabrication Method	Flexural Strength (MPa)	Notes
Kammler et al., 2021(90)	Standard sintered alumina	~356	High-density reference sample
Zhang et al., 2022 (75)	DLP + Sintering	250–300	Low porosity (~10%)
Ćurković et al., 2010 (91)	Sintered alumina	260–300	Weibull analysis on dense alumina
ASTM C1161 (85)	Standard Limit	>300	Dense commercial ceramics
This Study	DLP (Admaflex)	228.07	High porosity (~30%)

The primary reason for the reduced flexural strength in this study is the relatively high porosity (~30%) of the sintered ceramic parts. Porosity reduces the effective load-bearing area and introduces potential sites for crack initiation, particularly in brittle materials like alumina. Additionally, the geometry of the test bars, characterized by a short span and thin cross-section, may have influenced the internal stress distribution underloading, potentially promoting earlier fracture.

Other contributing factors include sintering-related variability, such as fluctuations in heating rate, dwell time, or peak temperature, which can affect grain growth and densification. Localized inhomogeneities may have led to inconsistent microstructures across samples, which in turn further impacted their mechanical response.

Minor imperfections during testing, such as sample misalignment, uneven seating, or small deviations in load application, can also be significant in brittle ceramics. Even slight misalignments can result in localized stress concentrations that trigger early failure.

Despite these challenges, the flexural strength data shows a relatively narrow statistical distribution, indicating a high level of repeatability in the printing and sintering process. With improved control over porosity, geometric tolerances, and test fixtures, the mechanical performance of DLP-fabricated alumina can be further enhanced, supporting its suitability for demanding structural applications.

3.3.2 Young's Modulus Evaluation

The elastic behavior of sintered alumina bars was investigated by calculating Young's modulus (E) based on three-point bending test data. The testing protocol followed the ASTM C1161 standard for advanced ceramics, using the same ten bar-shaped samples analyzed for flexural strength. The load-displacement curves were recorded for each specimen, and the slope of the initial linear elastic portion was extracted to compute the modulus.

To ensure reliable stiffness evaluation, the slope ($\Delta F/\Delta \delta$) was selected from the earliest, most linear segment of the force–displacement graph. This method isolates the purely elastic region and avoids interference from microcrack propagation, geometric nonlinearity, or fixture compliance.

Using the standard beam-bending equation for rectangular bars, the Young's modulus for each sample was calculated based on the extracted slope, support span, and pre-sintering dimensions. The resulting modulus values ranged from 205.1 to 240.5 GPa, with a mean of 221.62 GPa and a standard deviation of ±12.50 GPa. Figure 34 illustrates the distribution of the slope and Young's modulus values across the tested samples.

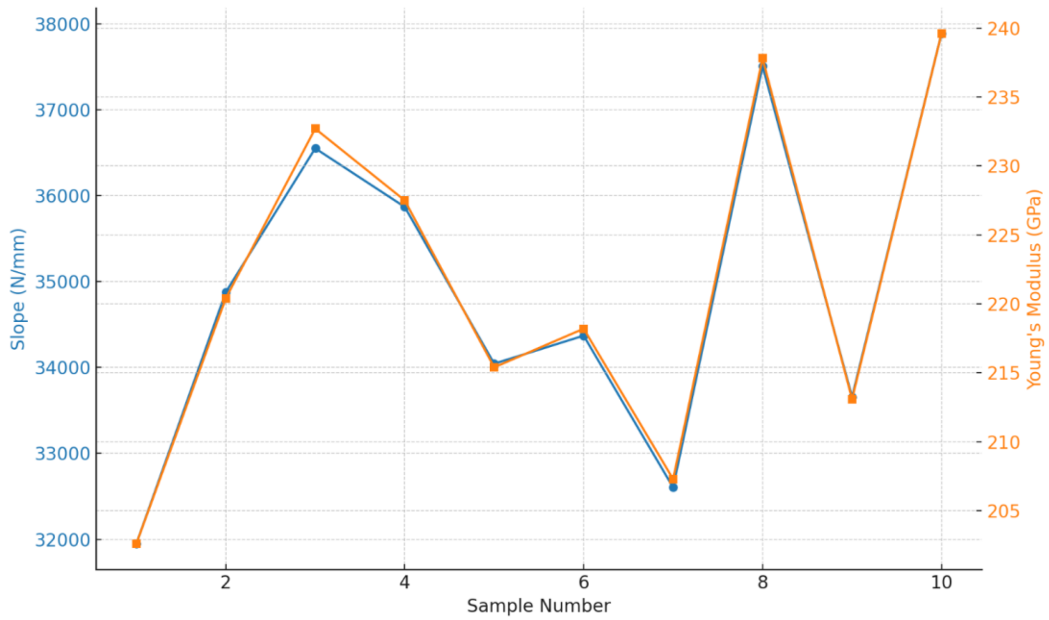

Figure 36. Slope and corresponding Young’s modulus for each of the ten tested alumina samples

A summary of the modulus-related parameters is presented in Table 13:

Table 13. Summary of Young’s modulus evaluation based on the three-point bending test

Parameter	Value	Unit	Notes
Number of Tested Samples	10	–	Derived from 14 printed specimens
Mean Young’s Modulus	221.62	GPa	Based on the linear slope of force–displacement
Young’s Modulus Standard Deviation	±12.50	GPa	Indicates stiffness variation
Mean Slope (ΔF/Δδ)	34,890.04	N/mm	Calculated from the linear elastic region
Slope Standard Deviation	±1,968.53	N/mm	Reflects the consistency of elastic response
Support Span (L)	14	mm	Constant test fixture setup
Width (b)	4	mm	Measured before sintering
Thickness (d)	3	mm	Measured before sintering
Testing Machine	INSTRON 2710-112	–	500 N load cell, standard 3PB configuration

These results fall within the expected range for moderately porous sintered alumina ceramics. Literature reports show that dense alumina typically exhibits Young's modulus values in the range of 260–400 GPa, depending on purity, grain size, and fabrication method.

Table 14. Literature Summary of Young's Modulus for Sintered and Additively Manufactured Alumina

Study	Fabrication Method	Young's Modulus (GPa)	Notes
Li et al., 2022 (75)	DLP + sintering	~270	Low porosity (~10%)
Schlacher et al., 2020(92)	Lithography-based AM (LCM)	260–280	Dense LCM alumina, low defect density
Ćurković et al., 2010 (91)	Sintered alumina with flaws	230–250	Non-dense samples with flaw sensitivity
AZoM Database [AZoM, 2023](93)	General alumina ceramics	215–413	Wide range depending on process & purity
This Study	DLP (Admaflex A13C) + sintering	221.62	~30% porosity, moderate elastic consistency

The lower modulus observed in this study is consistent with the ~30% porosity measured, which significantly reduces the stiffness due to reduced cross-sectional load transfer and increased internal voids.

Additional factors contributing to the variability and reduced modules include:

- Sample geometry effects, particularly the short span and reduced thickness of the printed bars.
- Surface misalignment during early loading, which may have introduced minor asymmetries in bending.
- Sintering variability, including localized grain coarsening or incomplete binder burnout.
- Measurement sensitivity at small displacements due to equipment resolution limits.

Nevertheless, the modules obtained show a relatively narrow distribution and align well with previous studies on DLP-fabricated ceramics, confirming the reproducibility and elastic integrity of the printed parts.

3.4 Thermal Conductivity Evaluation

Thermal characterization of the sintered alumina sample was conducted using the GHFM-01 Guarded Heat Flow Meter, following the ASTM E1530-19(88) standard. This steady-state method enables accurate measurement of thermal resistance (R) and thermal conductivity (λ) for solid materials under defined thermal gradients.

The alumina discs had a final diameter of approximately 49 mm and a thickness of 2 mm. Tests were conducted at four mean temperatures (100 °C, 150 °C, 200 °C, and 250 °C), each with a ±15 °C gradient between the upper and lower heating plates.

During testing, heat flux behavior was continuously monitored to verify the achievement of steady-state conditions before each measurement. This step ensured data reliability by confirming thermal equilibrium throughout the ceramic sample. At all temperature levels, a stable heat flux plateau was observed.

Table 15. Heat flux stability during thermal testing of alumina

Temp (°C)	Final Flux (approx.)	Steady-State Reached?	Duration
100	~7500–8000 W/m²	Yes	~1h15m
150	~7200 W/m²	Yes	~58 min
200	~6800–6900 W/m²	Yes	~38 min
250	~6600–6800 W/m²	Yes	~52 min

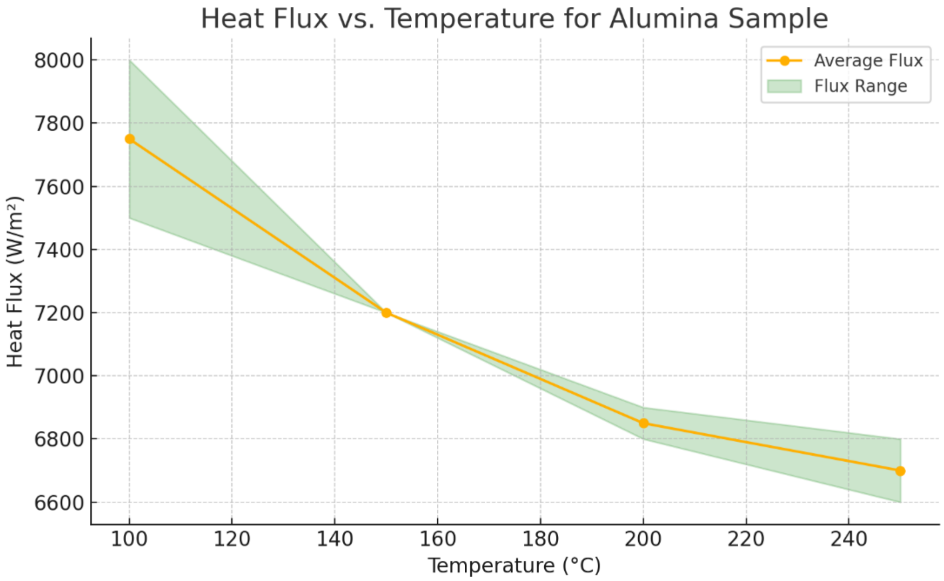

Figure 37. Average and range of steady-state heat flux values recorded at four mean temperatures during thermal conductivity testing of sintered alumina. The orange line shows the average flux; the green shaded region represents the min–max range.

The steady heat flux behavior confirmed the reliability of the thermal conductivity measurements. These experimentally derived values (Table 16) were later used in thermal simulation models to assess the performance of 3D-printed alumina as a thermal dissipator in electronic applications.

Table 16. Thermal conductivity and resistance values for sintered alumina

Mean Temp (°C)	Upper Temp	Lower Temp	TC (W/m·K)	R (m²K/W)	Thickness (mm)	Duration (min)
100	115	85	1.976	0.001123	2	80
150	165	135	2.163	0.001026	2	60
200	215	185	2.444	0.000908	2	40
250	265	235	2.395	0.000927	2	55

The thermal conductivity ranged from 1.98 W/m·K at 100 °C to a peak of 2.44 W/m·K at 200 °C, reflecting stable and favorable heat dissipation behavior consistent with that of porous ceramic materials. As expected, the associated thermal resistance values decreased with increasing temperature due to improved phonon transport.

While the measured values demonstrated coherent thermal trends, they were influenced by geometrical deviations from the ASTM E1530-19(88) standard. Specifically, this standard recommends that circular samples for guarded heat flow meter (GHFM) testing have diameters between 50.0 mm and 50.8 mm to ensure uniform heat flux coverage, minimize edge losses, and guarantee accurate thermal contact. This deviation is attributed to a combination of factors:

- Design constraints in the DLP printer's build platform, limiting initial CAD dimensions.
- Shrinkage during the debinding and sintering processes.
- Microstructural densification, driven by porosity evolution and grain boundary formation, which led to a ~1 mm reduction in final part size.

Although the specimens were flat and parallel, and thermal contact paste was applied to improve interface conductivity, this slight dimensional shortfall likely introduced minor but measurable thermal errors:

- Radial heat losses at the exposed edges, particularly significant at lower test temperatures (100–200 °C).
- Reduced contact area between the alumina disc and instrument plates, increasing the thermal contact resistance.
- Potential underestimation of bulk thermal conductivity due to disturbed axial heat transfer paths.

When compared with reference values for fully dense alumina, which typically show conductivity in the range of 25–30 W/m·K at room temperature (AZoM, 2023; ASTM C408) (93)The results obtained in this study are significantly lower. However, this discrepancy aligns with findings reported by Rezaee and Ranjbar (2020) (94) , where alumina composites with 17–65 vol% porosity exhibited a dramatic reduction in thermal conductivity, from approximately 11 W/m·K to as low as 2 W/m·K, representing a decrease of more than 80% in highly porous samples.

Although the samples were dimensionally stable and functional, the ~1 mm deviation in diameter from ASTM specifications likely introduced edge heat loss and imperfect contact conditions, contributing to a slight underestimation of the true thermal conductivity values.

Given these effects, the measured values are best interpreted as representative of moderately porous, geometrically non-ideal alumina, rather than directly comparable to industrial-grade reference materials. The data remains valid for simulation input and for assessing relative trends in ceramic heat dissipation performance under realistic AM constraints.

3.5 Numerical Simulation of a Ceramic Thermal Dissipator

The system's response to the thermal and flow stimuli described in the Materials and Methods section is here represented and discussed. The first output is the fluid flow behavior within the internal cylindrical channels of the ceramic dissipator. Specifically, we observe the velocity field through streamline plots, which illustrate how water flows through the embedded cooling paths.

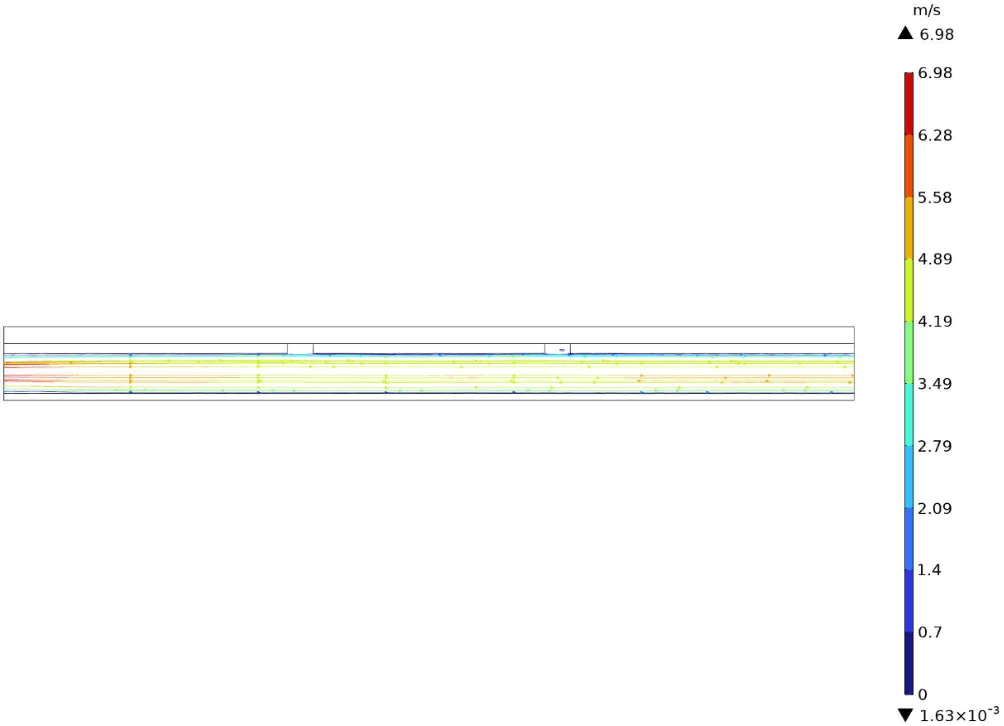

Figure 38. Velocity streamline plot of laminar water flow through the internal cylindrical channels of the ceramic dissipator (flow rate = 0.1 L/min at 25 °C).

As shown in Figure 38, the streamline visualization confirms the presence of laminar flow, as anticipated by the modeling assumptions. The maximum velocity recorded reaches approximately 7 m/s, which, although high, remains acceptable within the flow regime and geometric scale defined in the simulation.

The inlet is located on the left-hand side of the model, where streamlines are tightly spaced and colored red to orange, indicating higher fluid velocity. This behavior results from the water entering the system at full flow rate with minimal resistance. As the flow progresses through the cylindrical channels, the velocity decreases gradually, with cooler (blue-green) tones appearing toward the right-hand outlet.

A closer analysis reveals a non-uniform velocity distribution across each channel's cross-section. The velocity peaks at the center of the flow and drops near the wall boundaries. This behavior is characteristic of laminar flow and is due to viscous shear forces governed by the no-slip boundary condition. Fluid layers adjacent to the solid wall experience drag, while central streamlines maintain higher speeds due to the absence of direct contact with boundary surfaces.

This can be understood by visualizing each streamline as a thin fluid slice: layers that move next to one another interact with low internal friction, whereas the interface between fluid and solid experiences strong resistance. As a result, the streamwise velocity profile assumes a parabolic distribution, with a maximum in the center and tapering near the walls.

The figure confirms that the internal geometry of the ceramic dissipator supports directional and stable laminar flow throughout its structure. While minor variations may exist due to transitions between holes and sidewalls, the simulation shows no evidence of turbulence, recirculation, or stagnation zones under current operating conditions.

Overall, this result validates the model boundary conditions, including the defined flow rate, wall constraints, and laminar assumption. The simulation setup offers a reliable baseline from which future studies can explore non-laminar or high-pressure regimes, which should be investigated together with more extreme thermal or mechanical loads.

The thermal and mechanical properties used in the simulation are summarized in the table below. Material data for water and copper were taken from COMSOL's built-in material library under standard ambient conditions (95). The alumina ceramic properties were based on experimentally derived values, particularly for Young's modulus, to reflect the actual behavior of the sintered material.

Table 17. Thermo-mechanical properties of alumina used in the simulation, including experimentally derived values and standard parameters from COMSOL's material library(95)

Property	**Value**	**Unit**
Thermal Conductivity (Alumina)	Interpolated value	W/(m·K)
Density (Alumina)	2850	kg/m³
Heat Capacity (Alumina)	900	J/(kg·K)
Coefficient of Thermal Expansion	7.5×10^{-6}	1/K
Young's Modulus (Tested Alumina)	221.62×10^{9}	Pa
Poisson's Ratio	0.222	–

After analyzing the velocity field, the next result concerns the temperature distribution across the copper–alumina–fluid system. This reveals how heat generated by the copper plate is transferred through the ceramic body and ultimately dissipates into the internal water channels, under a 10 W steady-state thermal load.

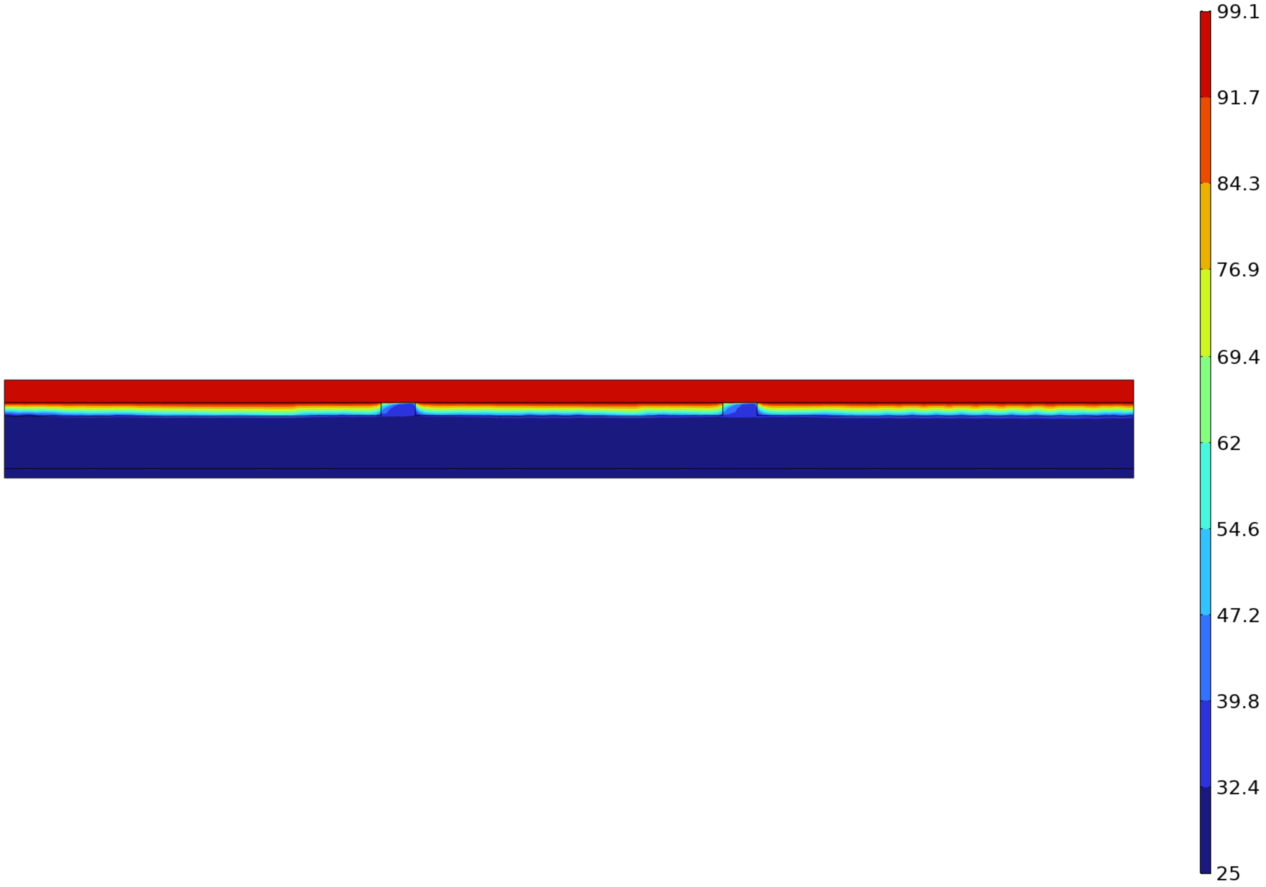

Figure 39. Cross-sectional temperature distribution across the full copper–alumina–fluid assembly.

In Figure 39, the copper plate is maintained at a constant temperature of approximately 99.1 °C, as imposed in the simulation to evaluate the thermal behavior of the alumina layer. This setup enables the analysis of how the uniform thermal load applied to the copper affects the temperature distribution within the ceramic component.

In contrast, the alumina layer exhibits a gradual and continuous temperature gradient from the top (in contact with copper) to the bottom (facing the water). Despite being in direct thermal contact with the copper, the bottom side of the alumina—where it interfaces with the fluid—only reaches approximately 44 °C. This confirms a substantial thermal resistance through the ceramic part.

This slow gradient confirms that heat transfer through the alumina is significantly impeded, as expected for a material with moderate thermal conductivity. The temperature change is not sharp or concentrated but rather diffused over the entire cross-section, reflecting alumina's insulating behavior. While this property can be advantageous in some electronic applications for isolating heat-sensitive zones, it may be a limitation when rapid heat dissipation is required, such as in high-power thermal management components.

To better understand potential improvements, the following plot presents a zoomed-in view of the region near the alumina–fluid interface. This visualization highlights a key limitation of the current geometry: although water is an effective coolant, the heat is not efficiently transferred to it due to the insulation of nature and thickness of the ceramic.

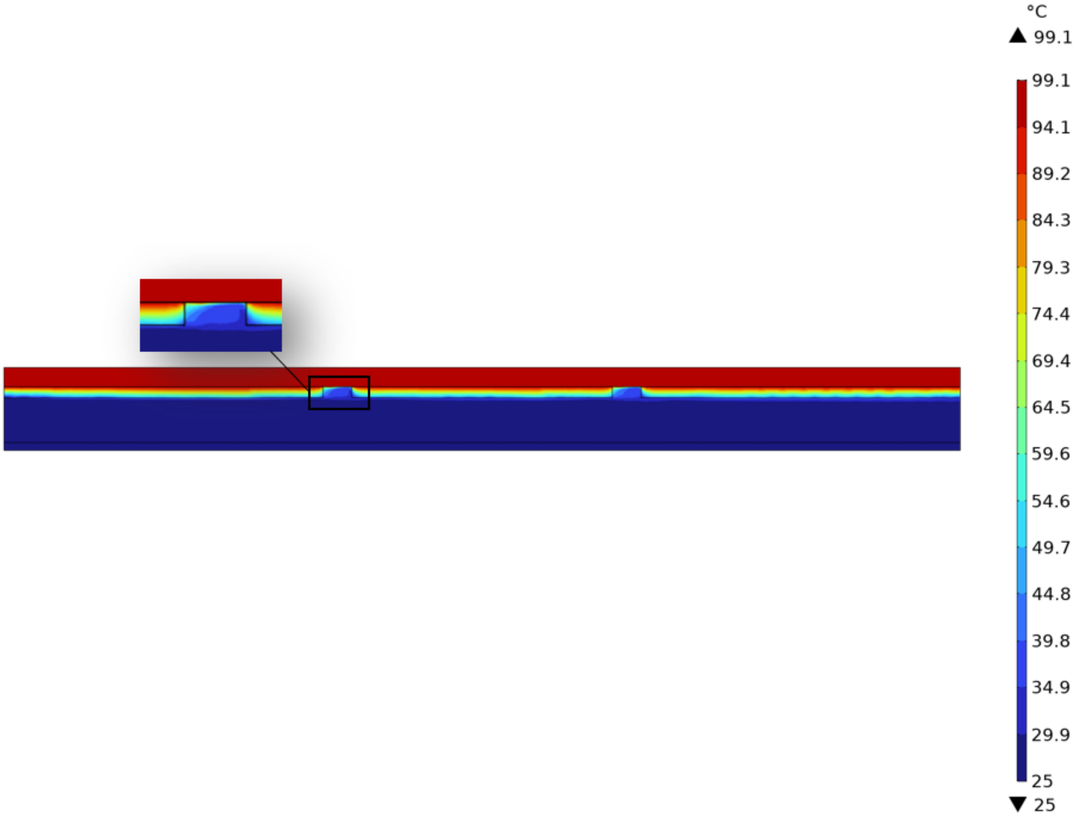

Figure 40. Zoomed-in temperature field near the alumina–fluid interface, used to explore potential design improvements.

From a design perspective, two improvement strategies can be identified:

- Reduce the thickness of the alumina layer: A thinner ceramic wall would shorten the conduction path, reduce thermal resistance, and accelerate heat transfer. However, this approach is constrained by fabrication limitations, including DLP resolution, minimum printable wall thickness, and structural stability during debinding or sintering.

- Enlarge or increase the number of water channels: Adding more channels or enlarging their diameter would enhance the contact area with the cooling fluid, increasing convective heat exchange. Yet, this must be balanced against mechanical robustness and the risk of structural weakening.

These changes aim to reduce the temperature drop across the ceramic, thereby lowering the system's effective thermal resistance. However, as is typical in thermal management applications, the optimal solution requires a trade-off between heat transfer efficiency, mechanical durability, and manufacturing feasibility.

A critical result of the simulation involves evaluating the mechanical displacement of the alumina plate under thermal loading. This analysis helps assess how the ceramic structure deforms when subjected to thermal expansion while being mechanically constrained along its edges.

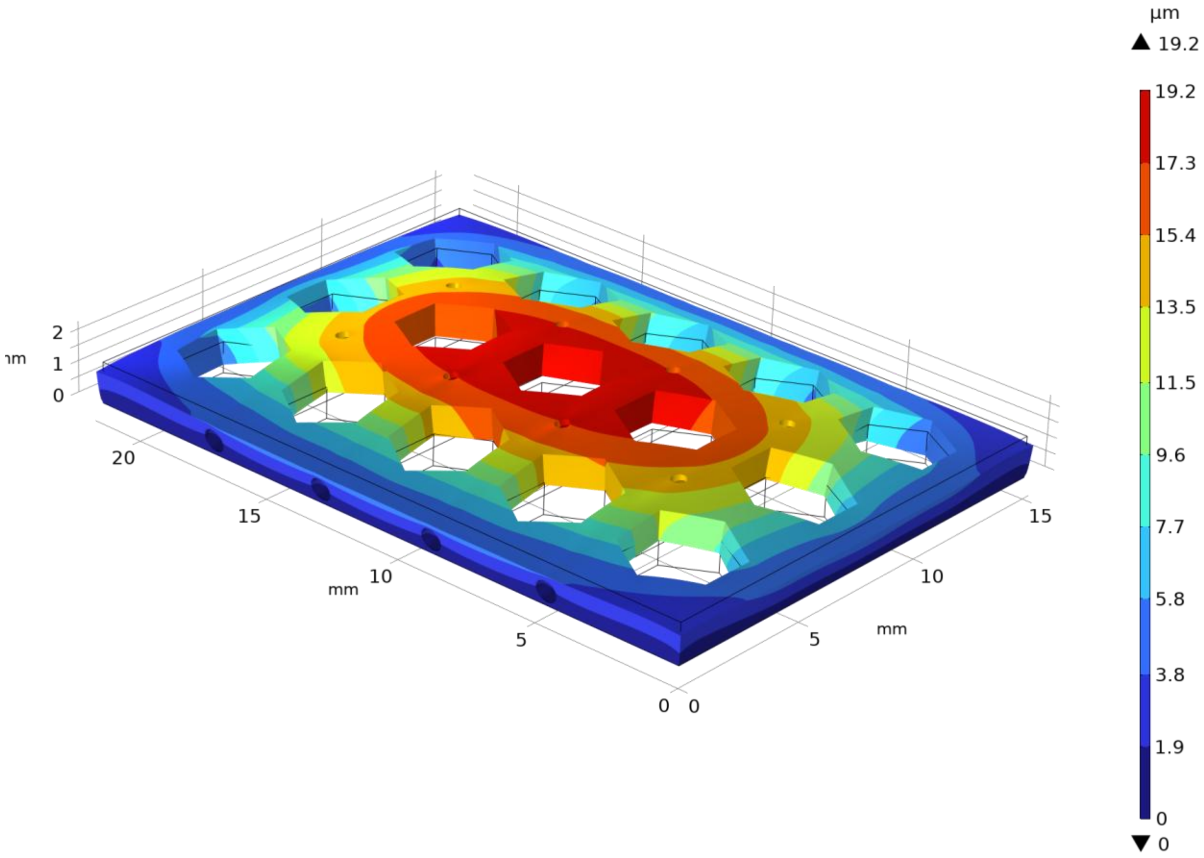

Figure 41. Mechanical displacement field of the alumina plate, resulting from thermal expansion and edge constraints. The color scale represents displacement magnitude in microns.

Figure 41 shows a classic bending deformation pattern, with the central region of the plate bulging outward due to thermal expansion resisted by the fixed boundaries. The temperature-induced strain accumulates most significantly in the middle, where the structure is free to deform. The displacement is smooth and symmetrical, reflecting the uniform nature of the applied thermal field and the symmetrical constraints.

Despite the apparent intensity of the color map, the actual maximum displacement is very small, measured at approximately 19 microns. This value confirms that the deformation remains within acceptable limits and does not compromise structural performance. The plate does not bend significantly, even though thermal expansion is present.

This result demonstrates that:

- The ceramic's mechanical response is governed by constraint placement and thermal load.
- Displacement is localized and controlled.
- The component's behavior under such thermal stress is stable and predictable.

Before analyzing the Von Mises stress distribution, it is important to review the mechanical boundary conditions applied to the alumina plate. The simulation considers a realistic scenario in which the ceramic component is mechanically supported along its outer edges, like how it would be mounted using screws or brackets in practical electronic assemblies.

These mechanical constraints were applied to accurately simulate thermal expansion effects while preserving realism. Rather than fixing entire surfaces or faces, which could result in an over-constrained model and suppress natural deformation, the simulation applies constraints only along the lines (edges) where the component would typically be physically supported.

This approach allows the ceramic plate to thermally expand, bend, and develop stress in response to internal temperature gradients, especially across the free central region. It also reflects actual mounting conditions, making the mechanical simulation more representative of real-world behavior.

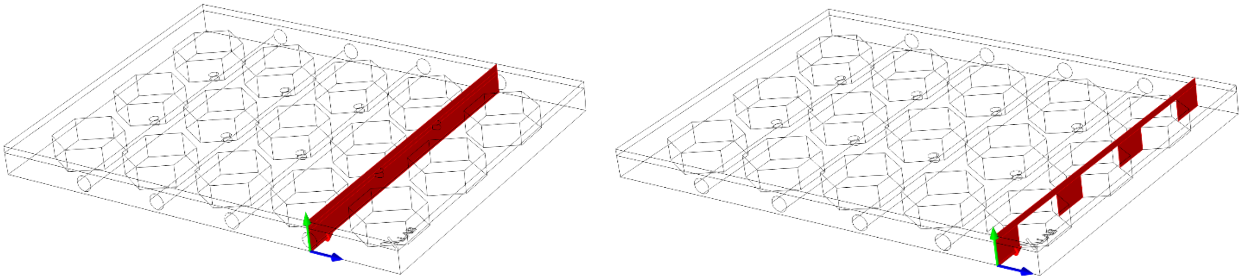

Figure 42 . Isometric views of the two cross-sectional planes used to visualize simulation results in the alumina plate: (left) transverse section and (right) longitudinal section.

Following the constraint configuration, the resulting von Mises stress distribution was evaluated to assess structural integrity under thermal loading.

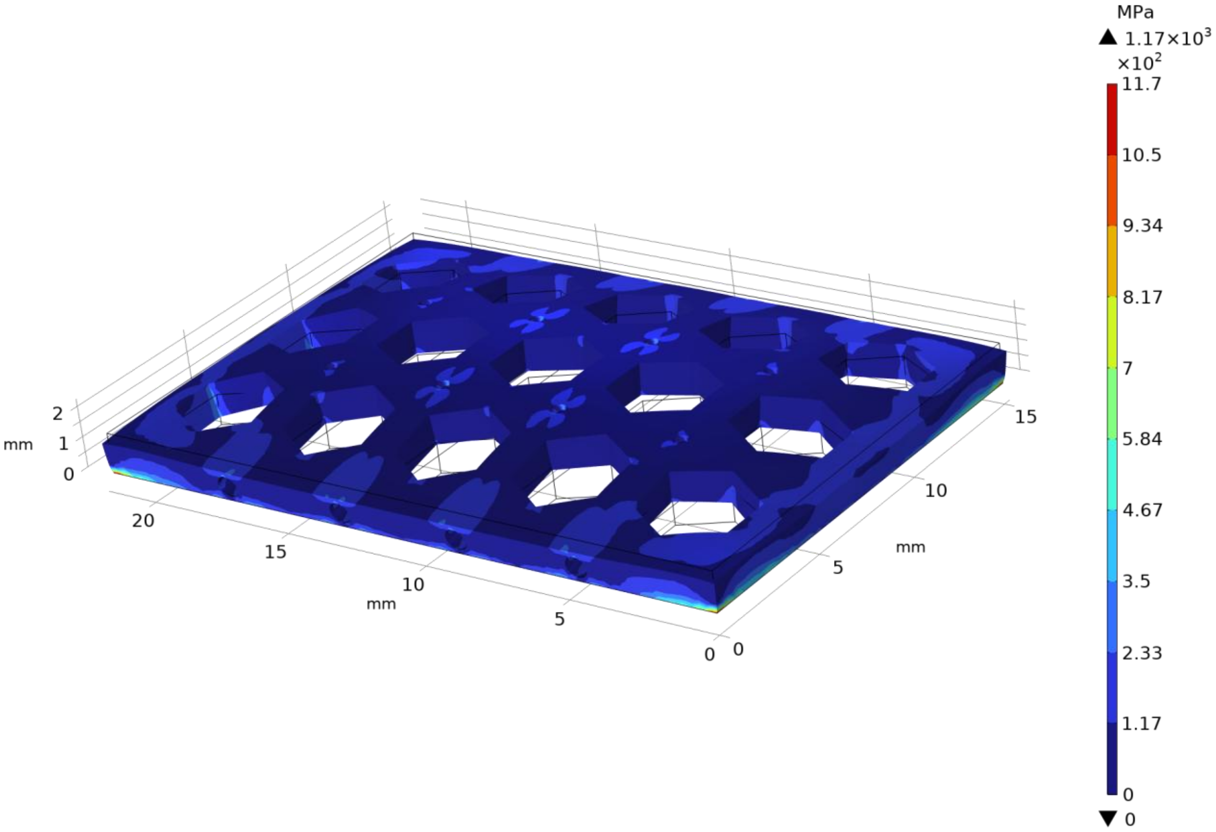

Figure 43. Von Mises stress field across the alumina plate under thermal expansion and edge-fixed boundary conditions.

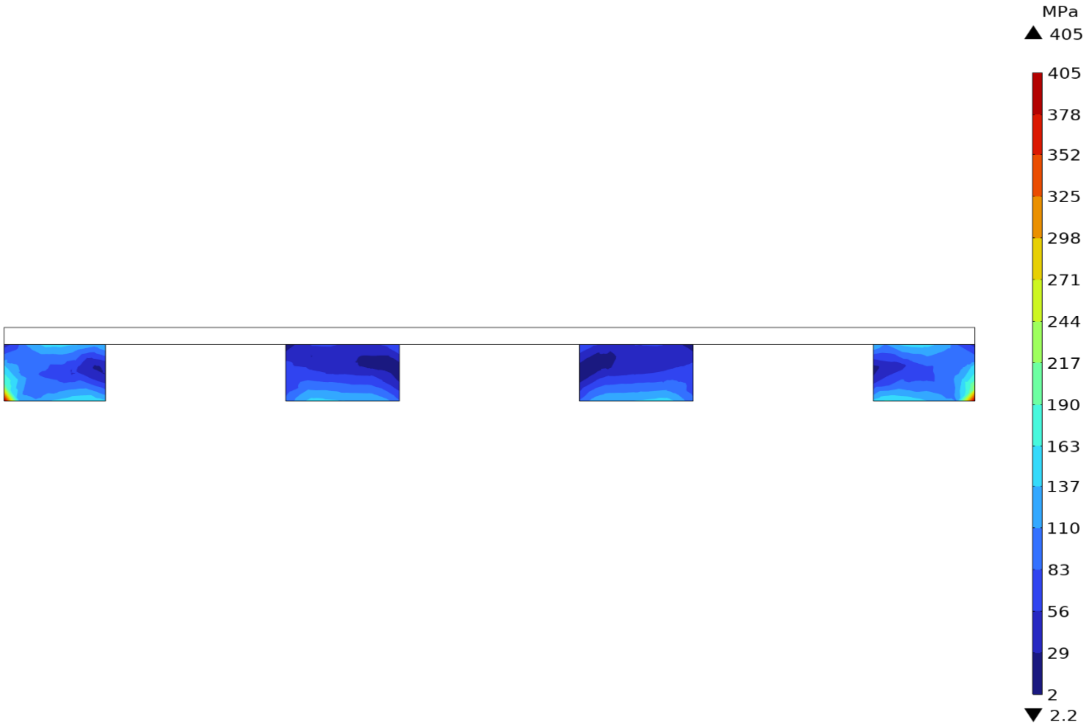

Figure 44. Von Mises stress profile extracted across the cross-section of the hexagonal cavities.

In Figure 43, areas near the four corners of the plate display localized red regions, suggesting high stress levels. However, these peaks are numerical artifacts, created by the mechanical constraints. They occur where the simulation restricts displacement too abruptly, leading to stress concentrations that do not reflect actual material failure risks.

More importantly, the stress distribution across the rest of the plate—including the central and functional regions—remains uniformly low, especially around the hexagonal holes where the geometry is most sensitive. This is confirmed by Figure 44, which displays the stress profile taken through the cross-sectional slices. It shows that most of the alumina plates experience stress levels on the order of ~1 MPa, far below critical fracture values for alumina ceramics under bending or tension.

These results confirm that:

- The structure is mechanically safe under the simulated thermal load.
- Constraint placement affects local results and must be interpreted with caution.
- The ceramic plate can accommodate expansion-induced stresses without critical failure, even with its complex geometry.

In conclusion, this simulation validates the mechanical integrity of the current design under the modeled thermal conditions and reinforces the importance of applying realistic mechanical constraints in finite element analyses to represent structural behavior accurately.

4 Conclusions

This study demonstrated the full process–structure–property relationship of ceramic components produced via Digital Light Processing (DLP) to fabricate sintered alumina parts for potential microelectronics and thermal management applications.

Key outcomes included:

- Dimensional Accuracy & Shrinkage: Final parts showed predictable shrinkage (~27.5% in height and ~55.9% volumetric), with reproducible geometrical fidelity.
- Porosity: Archimedes-based measurements revealed a total porosity of 29.6%, dominated by closed porosity (28.7%), indicating successful densification and minimal interconnected defects
- Mechanical Performance: Flexural strength averaged 228.1 MPa and Young's modulus 221.6 GPa, confirming that the parts retained adequate structural performance for non-load-bearing components. The mechanical behavior under three-point bending reflected the combined effect of porosity and micro-defects, showing robustness for applications where strength is not the primary constraint.
- Thermal Conductivity: Conductivity ranged from 1.98 W/m·K at 100 °C to 2.44 W/m·K at 200 °C, validating heat dissipation capabilities of the printed ceramics despite geometric non-ideality. In thermal testing, despite slight deviation from ASTM sample diameter requirements (49 mm vs 50 mm), steady-state conditions were reached, and results remained consistent with literature on porous ceramics.
- Simulation Results: A custom ceramic thermal dissipator was simulated in COMSOL, confirming mechanical stability under thermal expansion and predicting laminar internal coolant flow with clear velocity gradients and safe stress distributions. In simulation, von Mises stress and displacement distributions confirmed that the printed alumina structure can withstand thermomechanical loads typical of thermal management applications. A noteworthy observation emerged from the zoomed-in fluid–solid interface view: despite water's excellent cooling capability, heat was not effectively transmitted through the ceramic thickness. This suggests that further improvements in design (e.g., reduced wall thickness or conductive coatings) are essential for performance enhancement.

The mechanical and thermal results align with expectations for moderately porous ceramics fabricated via additive manufacturing. The lower stiffness and conductivity compared to dense alumina can be directly attributed to the ~30% internal porosity and sintering-induced microstructural changes.

In conclusion, the produced parts exhibit good dimensional reliability and reproducibility, and mechanical and thermal properties are consistent with moderately porous ceramics, suitable for passive support or insulation applications.

Furthermore, numerical modeling confirmed safe thermal operation and mechanical integrity of the alumina structure, even with complex geometries. This provides a replicable foundation for industrial adoption of DLP in thermal and structural ceramic applications.

Some limitations must be presented, like sample sizes deviation from ASTM specs, which can potentially introduce minor thermal error. Porosity measurement did not include detailed microstructural imaging (e.g., SEM/XCT correlation). The simulation was steady-state and did not consider transient heating or real flow turbulence.

That is the reason why future developments in this work could be:

- Optimize sintering to further reduce closed porosity and improve thermal conductivity.
- Design thinner, multi-material structures to enhance heat transfer across fluid interfaces.
- Extending simulation studies, including real thermal cycles, cyclic stress, or pulsating flow.
- Employ microstructural analysis to correlate defect size and distribution with mechanical failure.

Acknowledgments

I would like to express my deepest gratitude to Professor Scaltrito and Professor Bertana for their exceptional mentorship, scientific insight, and constant encouragement throughout the development of this thesis. Their expertise and critical feedback have been fundamental in shaping both the research direction and the outcome of this work.

I am especially thankful to my colleagues Matilde Aronne and Giulia Mossotti for their collaboration, shared knowledge, and invaluable support during the experimental activities and analysis phases. Their presence and teamwork have greatly enriched this experience.

Special thanks are extended to the Additive Manufacturing Laboratory (ChiLab) at Politecnico di Torino – Chivasso, not only for granting access to advanced facilities and instrumentation, but also for the generous support of the research staff, colleagues, and friends who contributed their time, expertise, and companionship throughout this journey.

Lastly, I am profoundly grateful to my family, whose unwavering love, sacrifices, and emotional support have sustained me at every stage of this academic path. Their belief in me has been a constant source of strength and motivation, and this accomplishment would not have been possible without them.

Bibliography

1. Darwish LR, El-Wakad MT, Farag MM. Towards sustainable industry 4.0: A green real-time IIoT multitask scheduling architecture for distributed 3D printing services. J Manuf Syst [Internet]. 2021;61:196–209. Available from: https://www.sciencedirect.com/science/article/pii/S0278612521001904
2. Gibson I, Rosen DW, Stucker B. Additive Manufacturing Technologies: 3D Printing, Rapid Prototyping, and Direct Digital Manufacturing [Internet]. 3rd ed. Springer; 2021. Available from: https://doi.org/10.1007/978-3-030-56127-7
3. Ngo TD, Kashani A, Imbalzano G, Nguyen KTQ, Hui D. Additive manufacturing (3D printing): A review of materials, methods, applications and challenges. Compos B Eng [Internet]. 2018;143:172–96. Available from: https://doi.org/10.1016/j.compositesb.2018.02.012
4. Sun H, Pedrielli G, Zhao G, Zhou C, Xu W, Pan R. Cyber coordinated simulation for distributed multi-stage additive manufacturing systems. J Manuf Syst [Internet]. 2020;57:61–71. Available from: https://www.sciencedirect.com/science/article/pii/S0278612520301278
5. Yi L, Gläßner C, Aurich JC. How to integrate additive manufacturing technologies into manufacturing systems successfully: A perspective from the commercial vehicle industry. J Manuf Syst [Internet]. 2019;53:195–211. Available from: https://www.sciencedirect.com/science/article/pii/S0278612519300792
6. Najmon JC, Raeisi S, Tovar A. 2 - Review of additive manufacturing technologies and applications in the aerospace industry. In: Froes F, Boyer R, editors. Additive Manufacturing for the Aerospace Industry [Internet]. Elsevier; 2019. p. 7–31. Available from: https://www.sciencedirect.com/science/article/pii/B9780128140628000029
7. Klotz UE, Tiberto D, Held F. Optimization of 18-karat yellow gold alloys for the additive manufacturing of jewelry and watch parts. Gold Bull [Internet]. 2017;50(2):111–21. Available from: https://doi.org/10.1007/s13404-017-0201-4
8. Bos F, Rob W, Zeeshan A, and Salet T. Additive manufacturing of concrete in construction: potentials and challenges of 3D concrete printing. Virtual Phys Prototyp [Internet]. 2016 Jul 2;11(3):209–25. Available from: https://doi.org/10.1080/17452759.2016.1209867
9. 261 I, F42 AC, 438 C. ISO/ASTM 52900:2021(En), Additive Manufacturing—General Principles—Fundamentals and Vocabulary. Geneva, Switzerland: International Organization for Standardization (ISO); 2021.
10. Gao W, Zhang Y, Ramanujan D, Ramani K, Chen Y, Williams CB, et al. The status, challenges, and future of additive manufacturing in engineering. Computer-Aided Design [Internet]. 2015;69:65–89. Available from: https://www.sciencedirect.com/science/article/pii/S0010448515000469
11. Zhang F, Wei M, Viswanathan V V, Swart B, Shao Y, Wu G, et al. 3D printing technologies for electrochemical energy storage. Nano Energy [Internet]. 2017;40:418–31. Available from: https://www.sciencedirect.com/science/article/pii/S221128551730513X

12. Duan J, Zhang Z, Zhu Y, Zhang F. Vat photopolymerization-based 3D printing of ceramics: A review. Ceram Int [Internet]. 2020;46(17):27313–33. Available from: https://doi.org/10.1016/j.ceramint.2020.07.199

13. Zhang F, Zhu L, Li Z, Wang S, Shi J, Tang W, et al. The recent development of vat photopolymerization: A review. Addit Manuf [Internet]. 2021;48:102423. Available from: https://www.sciencedirect.com/science/article/pii/S2214860421005753

14. Melchels FPW, Feijen J, Grijpma DW. A review on stereolithography and its applications in biomedical engineering. Biomaterials [Internet]. 2010;31(24):6121–30. Available from: https://doi.org/10.1016/j.biomaterials.2010.04.050

15. Stampfl J, Schwentenwein M, Homa J, Prinz FB. Lithography-based additive manufacturing of ceramics: Materials, applications and perspectives. MRS Commun [Internet]. 2023;13(5). Available from: https://doi.org/10.1557/s43579-023-00444-0

16. Tumbleston JR, Shirvanyants D, Ermoshkin N, Janusziewicz R, Johnson AR, Kelly D, et al. Continuous liquid interface production of 3D objects. Science (1979). 2015;347(6228):1349–52.

17. Yilmaz B, Al Rashid A, Mou YA, Evis Z, Koç M. Bioprinting: A review of processes, materials and applications. Bioprinting [Internet]. 2021;23:e00148. Available from: https://www.sciencedirect.com/science/article/pii/S240588662100021X

18. Huang B, Hu R, Xue Z, Zhao J, Li Q, Xia T, et al. Continuous liquid interface production of alginate/polyacrylamide hydrogels with supramolecular shape memory properties. Carbohydr Polym [Internet]. 2020;231:115736. Available from: https://www.sciencedirect.com/science/article/pii/S0144861719314043

19. Redwood B, Schoöffer F, Garet B. The 3D Printing Handbook: Technologies, Design and Applications. Amsterdam: 3D Hubs; 2017.

20. Wang L, Luo Y, Yang Z, Dai W, Liu X, Yang J, et al. Accelerated refilling speed in rapid stereolithography based on nano-textured functional release film. Addit Manuf [Internet]. 2019;29:100791. Available from: https://www.sciencedirect.com/science/article/pii/S2214860419302969

21. Desimone J, Alexander M, Nikita E, Edward E, Smulski T. Continous Liquid Interphase Printing. U.S. Patent Office; 2014.

22. Bártolo P. Stereolithography: Materials, Processes and Applications. New York, NY, USA: Springer; 2011.

23. Mu Q, Wang L, Dunn CK, Kuang X, Duan F, Zhang Z, et al. Digital light processing 3D printing of conductive complex structures. Addit Manuf [Internet]. 2017;18:74–83. Available from: https://www.sciencedirect.com/science/article/pii/S2214860417300398

24. Kadry H, Wadnap S, Xu C, Ahsan F. Digital light processing (DLP) 3D-printing technology and photoreactive polymers in fabrication of modified-release tablets. European Journal of Pharmaceutical Sciences [Internet]. 2019;135:60–7. Available from: https://www.sciencedirect.com/science/article/pii/S0928098719301794

25. Li Y, Mao Q, Yin J, Wang Y, Fu J, Huang Y. Theoretical prediction and experimental validation of the digital light processing (DLP) working curve for photocurable materials. Addit Manuf [Internet]. 2021;37:101716. Available from: https://www.sciencedirect.com/science/article/pii/S2214860420310885

26. Deckers J, Vleugels J, Kruth JP. Additive manufacturing of ceramics: A review. Journal of Ceramic Science and Technology [Internet]. 2014;5(4):245–60. Available from: https://doi.org/10.4416/JCST2014-00032

27. Schwarzer E, Götz M, Markova D, Stafford D, Scheithauer U, Moritz T. Lithography-based ceramic manufacturing (LCM) – Viscosity and cleaning as two quality influencing steps in the process chain of printing green parts. J Eur Ceram Soc [Internet]. 2017;37(16):5329–38. Available from: https://www.sciencedirect.com/science/article/pii/S0955221917303990

28. Travitzky N, Bonet A, Dermeik B, Fey T, Filbert-Demut I, Schlier L, et al. Additive manufacturing of ceramic-based materials. Adv Eng Mater. 2014;16(6):729–54.

29. Stansbury JW, Idacavage MJ. 3D printing with polymers: Challenges among expanding options and opportunities. Dental Materials [Internet]. 2016;32(1):54–64. Available from: https://www.sciencedirect.com/science/article/pii/S0109564115004145

30. Phillips R. Photopolymerization. Journal of Photochemistry [Internet]. 1984;25(1):79–82. Available from: https://www.sciencedirect.com/science/article/pii/0047267084850169

31. Mendes-Felipe C, Oliveira J, Etxebarria I, Vilas-Vilela JL, Lanceros-Mendez S. State-of-the-Art and Future Challenges of UV Curable Polymer-Based Smart Materials for Printing Technologies. Adv Mater Technol [Internet]. 2019;4(3):1800618. Available from: https://doi.org/10.1002/admt.201800618

32. Pagac M, Hajnys J, Ma QP, Jancar L, Jansa J, Stefek P, et al. A Review of Vat Photopolymerization Technology: Materials, Applications, Challenges, and Future Trends of 3D Printing. Polymers (Basel). 2021;13(4):598.

33. Fiedor P, Pilch M, Szymaszek P, Chachaj-Brekiesz A, Galek M, Ortyl J. Photochemical Study of a New Bimolecular Photoinitiating System for Vat Photopolymerization 3D Printing Techniques Under Visible Light. Catalysts. 2020;10(3):284.

34. Crivello J, Reichmanis E. Photopolymer Materials and Processes for Advanced Technologies. Chemistry of Materials. 2014;26(1):533–48.

35. Badev A, Abouliatim Y, Chartier T, Lecamp L, Lebaudy P, Chaput C, et al. Photopolymerization kinetics of a polyether acrylate in the presence of ceramic fillers used in stereolithography. J Photochem Photobiol A Chem [Internet]. 2011;222(1):117–22. Available from: https://www.sciencedirect.com/science/article/pii/S1010603011002243

36. Dendukuri D, Panda P, Haghgooie R, Kim JM, Hatton TA, Doyle PS. Modeling of Oxygen-Inhibited Free Radical Photopolymerization in a PDMS Microfluidic Device. Macromolecules. 2008;41(22):8547–56.

37. Pan X, Tasdelen MA, Laun J, Junkers T, Yagci Y, Matyjaszewski K. Photomediated Controlled Radical Polymerization. Prog Polym Sci. 2016;62:73–125.

38. Hussain MI, Xia M, Ren XN, Gupta MK, Others. Digital light processing 3D printing of ceramic materials: A review on basic concept, challenges, and applications. The International Journal of Advanced Manufacturing Technology. 2023;130(5–6):1–27.

39. Manapat JZ, Chen Q, Ye P, Advincula RC. 3D Printing of Polymer Nanocomposites via Stereolithography. Macromol Mater Eng. 2017;

40. Schwentenwein M, Homa J. Additive manufacturing of dense alumina ceramics. Int J Appl Ceram Technol [Internet]. 2015;12(1):1–7. Available from: https://doi.org/10.1111/ijac.12339

41. Eisenbach I. Ceramics. In: English for Materials Science and Engineering. Vieweg+Teubner; 2011. p. 40–50.

42. Lu M, Zhao Z. Additive Manufacturing of Alumina-Based Ceramic Structures by Vat Photopolymerization: A Scoping Review. Materials [Internet]. 2024;18(11):2445. Available from: https://www.mdpi.com/1996-1944/18/11/2445

43. Zocca A, Colombo P, Gomes CM, Günster J. Additive manufacturing of ceramics: Issues, potentialities, and opportunities. Journal of the American Ceramic Society. 2015;98(7):1983–2001.

44. Gao X, Chen J, Chen X, Wang W, Li Z, He R. How to Improve the Curing Ability During the Vat Photopolymerization 3D Printing of Non-Oxide Ceramics: A Review. Materials. 2024;17(11):2626.

45. Camargo IL de, al. et. A review on the rheological behavior and formulations of ceramic suspensions for vat photopolymerization. Ceram Int [Internet]. 2021; Available from: https://doi.org/10.1016/j.ceramint.2021.03.071

46. Miao WJ, Wang SQ, Wang ZH, Wu FB, Zhang YZ, Ouyang JH, et al. Additive Manufacturing of Advanced Structural Ceramics for Tribological Applications: Principles, Techniques, Microstructure and Properties. Lubricants [Internet]. 2025;13(3):112. Available from: https://doi.org/10.3390/lubricants13030112

47. Eblen DR. Thermal Conductivity of Thick Film Tungsten Metallization Used in High-Alumina Ceramic Microelectronic Packages [Internet]. Semantic Scholar; 2015. Available from: https://www.semanticscholar.org/paper/Thermal-Conductivity-of-Thick-Film-Tungsten-used-in-Eblen/31704181c39807e8b5974ac2d4c08e11b54f52ac

48. Bai R, Sun Q, He Y, Peng L, Zhang Y, Zhang L, et al. Ceramic Toughening Strategies for Biomedical Applications. Front Bioeng Biotechnol. 2022;10:840372.

49. Winser M. A Single package X-Band T/R module. In: 35th European Microwave Conference. Session EuM23 Module Packaging; 2005. p. 493–6.

50. Entezari A, Roohani-Esfahani SI, Zhang Z, Zreiqat H, Dunstan CR, Li Q. Fracture behaviors of ceramic tissue scaffolds for load bearing applications. Sci Rep [Internet]. 2016;6(1):28816. Available from: https://doi.org/10.1038/srep28816

51. Kong N, Chen A, Yan W, Zhang H. Ceramic Implant Fracture: A Clinical Report. Journal of Prosthetic Dentistry. 2019;122(5):425–9.

52. Verma V, and Kumar BVM. Processing of alumina-based composites via conventional sintering and their characterization. Materials and Manufacturing Processes [Internet]. 2017 Jan 2;32(1):21–6. Available from: https://doi.org/10.1080/10426914.2016.1198023

53. He L, Liu Y, Liu Y, Hu K, Lu Z, Liang J. Effects of Solvent Debinding on the Microstructure and Properties of 3D-Printed Alumina Ceramics. ACS Omega [Internet]. 2020;5(42):27455–62. Available from: https://doi.org/10.1021/acsomega.0c03944

54. Zhou S, Liu G, Wang C, Zhang Y, Yan C, Shi Y. Thermal debinding for stereolithography additive manufacturing of advanced ceramic parts: A comprehensive review. Mater Des

[Internet]. 2024;238:112632. Available from: https://www.sciencedirect.com/science/article/pii/S0264127524000042

55. Liu G, Yan C, Zhang K, Jin H, He R. Effect of Solid Loading on the Property of Al_2O_3 Ceramics in Stereolithographic Additive Manufacturing. Journal of Inorganic Materials. 2022;37(3):353–60.

56. Jin F, Li Q, Yang K, Qiu Y, Fan J. Optimisation and application of high solid loading stereolithography 3D printing ceramic cores slurry. Ceram Int. 2023;49(24):6867–78.

57. (VDI) VDI. VDI 3405 Blatt 8.1 (2021). Additive manufacturing processes – Design rules – Parts using ceramic materials. Düsseldorf, Germany: VDI; 2021.

58. Chaudhary R, Fabbri P, Leoni E, Mazzanti F, Akbari R, Antonini C. Additive manufacturing by digital light processing: a review. Progress in Additive Manufacturing [Internet]. 2023;8(2):331–51. Available from: https://doi.org/10.1007/s40964-022-00336-0

59. Mamatha S, Biswas P, Johnson R. Digital light processing of ceramics: an overview on process, materials and challenges. Progress in Additive Manufacturing [Internet]. 2022;8:1083–102. Available from: https://doi.org/10.1007/s40964-022-00303-5

60. Zhou L, Miller J, Vezza J, Mayster M, Raffay M, Justice Q, et al. Additive Manufacturing: A Comprehensive Review. Sensors [Internet]. 2024;24(9):2668. Available from: https://doi.org/10.3390/s24092668

61. Swetha S, Sahiti TJ, Priya GS, Anil A, Others. Review on digital light processing (DLP) and effect of printing parameters on quality of print. Interactions. 2024;245(1).

62. Andreu A, Su PC, Kim JH, Ng CS, Kim S, Kim I, et al. 4D Printing Materials for Vat Photopolymerization. Addit Manuf. 2021;44:102024.

63. Wang JC, Dommati H, Hsieh SJ. Review of additive manufacturing methods for high-performance ceramic materials. The International Journal of Advanced Manufacturing Technology [Internet]. 2019;103(5):2627–47. Available from: https://doi.org/10.1007/s00170-019-03669-3

64. Saroia J, Wang Y, Wei Q, Lei M, Li X, Guo Y, et al. A review on 3D printed matrix polymer composites: its potential and future challenges. The International Journal of Advanced Manufacturing Technology [Internet]. 2020;106(5):1695–721. Available from: https://doi.org/10.1007/s00170-019-04534-z

65. Myles A, Griffith A, Riyad MF, Minary-Jolandan M. 3D-Printed Ceramics with Aligned Micro-Platelets. ACS Appl Energy Mater [Internet]. 2023;1(7). Available from: https://doi.org/10.1021/acsaenm.3c00223

66. Bove A, Calignano F, Galati M, Iuliano L. Photopolymerization of Ceramic Resins by Stereolithography Process: A Review. Applied Sciences [Internet]. 2022;12(7):3591. Available from: https://doi.org/10.3390/app12073591

67. Li M, Huang Y, Zhang Y, Xu Y. Optimization of sintering temperature for DLP-printed alumina ceramics: Effects on porosity and mechanical strength. J Eur Ceram Soc. 2023;43(1):89–97.

68. Ryu K, Kim J, Choi J, Kim U. The 3D Printing Behavior of Photocurable Ceramic/Polymer Composite Slurries Prepared with Different Particle Sizes. Nanomaterials [Internet]. 2022;12(15):2631. Available from: https://doi.org/10.3390/nano12152631

69. Thakur T, Carretta M, Komissarenko D, Blugan G. Advancements in DLP 3D Printing: High Strength Alumina Toughened Zirconia Ceramics for Biomedical Applications. Open Ceramics [Internet]. 2024;18(7). Available from: https://doi.org/10.1016/j.oceram.2024.100601

70. Diao Q, Zeng Y, Chen J. The Applications and Latest Progress of Ceramic 3D Printing. Additive Manufacturing Frontiers [Internet]. 2024;3(1):200113. Available from: https://www.sciencedirect.com/science/article/pii/S2950431724000042

71. Bose S, Akdogan EK, Balla VK, Ciliveri S, Colombo P, Franchin G, et al. 3D printing of ceramics: Advantages, challenges, applications, and perspectives. Journal of the American Ceramic Society [Internet]. 2024; Available from: https://doi.org/10.1111/jace.20043

72. Čelko L, Gutiérrez-Cano V, Casas-Luna M, Matula J, Oliver-Urrutia C, Remešová M, et al. Characterization of porosity and hollow defects in ceramic objects built by extrusion additive manufacturing. Addit Manuf. 2021;47:102272.

73. Wang G, Ma C, Hu T, Wang T. Ceramic 3D printing via dye-sensitized photopolymerization under green LED. 3D Print Addit Manuf. 2023;10(2):310–7.

74. Truxova V, Safka J, Seidl M, Kovalenko I, Volesky L, Ackermann M. Ceramic 3D Printing: Comparison of SLA and DLP Technologies. MM Science Journal. 2020;(06):3704–9.

75. Li Q, An X, Liang J, Liu Y, Hu K, Lu Z, et al. Balancing flexural strength and porosity in DLP-3D printing Al2O3 cores for hollow turbine blades. J Mater Sci Technol [Internet]. 2022;104:19–32. Available from: https://www.sciencedirect.com/science/article/pii/S1005030221006617

76. Rane K, Petrò S, Strano M. Evolution of porosity and geometrical quality through the ceramic extrusion additive manufacturing process stages. Addit Manuf [Internet]. 2020;32:101038. Available from: https://www.sciencedirect.com/science/article/pii/S2214860419317257

77. Hwa LC, Rajoo S, Noor AM, Ahmad N, Uday MB. Recent advances in 3D printing of porous ceramics: A review. Curr Opin Solid State Mater Sci [Internet]. 2017;21(6):323–47. Available from: https://www.sciencedirect.com/science/article/pii/S1359028616301723

78. Lee J, Kim S, Park J. Effects of debinding condition on microstructure and densification of alumina ceramics shaped with photopolymerization-based additive manufacturing technology [Internet]. ResearchGate; 2022. Available from: https://www.researchgate.net/publication/358215916

79. Jayaweera JMN, Narayana M, Adikary SU. Modeling and Simulation of Ceramic Tiles Linear Shrinkage Variation During the Sintering Process. Forces in Mechanics. 2024;15:100274.

80. Qian C, Hu K, Lu Z, Li P. Volume Shrinkage and Conversion Rate of Al_2O_3 Ceramic Stereolithography Suspension Polymerised by Ultraviolet Light. Mater Chem Phys. 2021;267:124661.

81. Chandan PB, Sankar MR. Extrusion-based additive manufacturing of alumina ceramics through controlled extrusion pressure. Int J Appl Ceram Technol [Internet]. 2024; Available from: https://doi.org/10.1111/ijac.14935

82. Sathiyakumar M, Gnanam FD. Influence of Additives on Density, Microstructure and Mechanical Properties of Alumina. J Mater Process Technol. 2003;133(3):282–6.

83. Du J, Ai D, Xiao X, Song J, Li Y, Chen Y, et al. Rational Design and Porosity of Porous Alumina Ceramic Membrane for Air Bearing. National Library of Medicine. 2024;

84. International A. ASTM C773-88(2020): Standard Test Method for Compressive (Crushing) Strength of Fired Whiteware Materials [Internet]. West Conshohocken, PA: ASTM International; 2020. Available from: https://www.astm.org/c0773-88r20.htm

85. International A. Standard Test Method for Flexural Strength of Advanced Ceramics at Ambient Temperature (ASTM C1161-18) [Internet]. ASTM International; 2018. Available from: https://www.scribd.com/document/779697414/ASTM-C1161-18

86. Callister WD, Rethwisch DG. Materials Science and Engineering: An Introduction [Internet]. 9th ed. Hoboken, NJ: John Wiley & Sons; 2014. Available from: https://anupturnedworld.files.wordpress.com/2017/08/callister-materials-science-and-engineering-9th-ed.pdf

87. Chawla KK. Ceramic Matrix Composites [Internet]. 2nd ed. New York, NY: Springer Science+Business Media; 2013. Available from: https://btpm.nmu.org.ua/students/subject/CeramicMatrixComposites_Chawla.pdf

88. International A. ASTM E1530-19: Standard Test Method for Evaluating the Resistance to Thermal Transmission by the Guarded Heat Flow Meter Technique [Internet]. West Conshohocken, PA: ASTM International; 2019. Available from: https://www.astm.org/e1530-19.html

89. comsol_single_phase_flow_https://www.comsol.com/blogs/using-the-material-libraries-in-comsol-multiphysics.

90. Kammler D, Cillessen DE, Ford KR, Larkin EC, Davidson WM, Christopher JM, et al. Flexural strength of a conventionally processed and additively manufactured debased 94% alumina. Int J Appl Ceram Technol [Internet]. 2021;19(3):1640–9. Available from: https://doi.org/10.1111/ijac.13968

91. Ćurković L, Bakić A, Kodvanj J, Haramina T. Flexural strength of alumina ceramics: Weibull analysis. Transactions of FAMENA. 2010;34(1):13–9.

92. Schlacher J, Lube T, Harrer W, Mitteramskogler G, Schwentenwein M, Danzer R, et al. Strength of additive manufactured alumina. J Eur Ceram Soc [Internet]. 2020;40(14):4737–45. Available from: https://doi.org/10.1016/j.jeurceramsoc.2020.03.073

93. Database AzM. Alumina (Al_2O_3) – Properties, Applications, Price and Suppliers [Internet]. AZoNetwork; 2023. Available from: https://www.azom.com/article.aspx?ArticleID=53

94. Rezaee S, Ranjbar K. Thermal conductivity of porous alumina–zirconia ceramic composites. Ceram Int [Internet]. 2020;46(3):3485–93. Available from: https://doi.org/10.1016/j.ceramint.2020.03.224

95. COMSOL_Material_Libraries_ https://doc.comsol.com/5.5/doc/com.